

A global study of NDVI difference among moderate-resolution satellite sensors

Xingwang Fan ^{a,b}, Yuanbo Liu ^{a,*}

^a Nanjing Institute of Geography and Limnology, Chinese Academy of Sciences, Nanjing 210008, China

^b Key Laboratory of Watershed Geographic Sciences, Chinese Academy of Sciences, Nanjing 210008, China



ARTICLE INFO

Article history:

Received 28 October 2015

Received in revised form 19 August 2016

Accepted 13 September 2016

Available online 15 October 2016

Keywords:

NDVI difference

LULC

AVHRR

MODIS

VIIRS

ABSTRACT

Moderate-resolution sensors, including AVHRR (Advanced Very High Resolution Radiometer), MODIS (MODerate-resolution Imaging Spectroradiometer) and VIIRS (Visible-Infrared Imager-Radiometer Suite), have provided over forty years of global scientific data. In the form of NDVI (Normalized Difference Vegetation Index), these data greatly benefit environmental studies. However, their usefulness is compromised by sensor differences. This study investigates the global NDVI difference and its spatio-temporal patterns among typical moderate-resolution sensors, as supported by state-of-the-art remote sensing derived products. Our study demonstrates that the atmosphere plays a secondary role to LULC (Land Use/Land Cover) in inter-sensor NDVI differences. With reference to AVHRR/3, AVHRR/1 and 2 exhibit negative NDVI biases for vegetated land cover types. In summer (July), the area of negative bias shifts northward, and the magnitude increases in the Northern Hemisphere. For most LULC types, the bias generally shifts in the negative direction from winter (January) to summer. A linear regression of the NDVI difference versus NDVI shows a close correlation between the slope value and vegetation phenology. Overall, NDVI differences are controlled by LULC type and vegetation phenology. Our study can be used to generate a long-term, consistent NDVI data set from composite MODIS and AVHRR NDVI data. LULC-dependent and temporally variable correction equations are recommended to reduce inter-sensor NDVI differences.

© 2016 International Society for Photogrammetry and Remote Sensing, Inc. (ISPRS). Published by Elsevier B.V. All rights reserved.

1. Introduction

Satellite sensors have accumulated over forty years of scientific data that meet the critical demands of the scientific community (Gutman and Ignatov, 1998; Ricotta et al., 1999; Lunetta et al., 2006; Wu et al., 2013). These data are affected by the atmosphere and generally need to be corrected for atmospheric effects (Rahman and Dedieu, 1994; Vermote et al., 1997; Tachiri, 2005). Transforming satellite data into spectral indexes provides an alternative means of reducing atmospheric effects (Gutman, 1991; Huete et al., 2002; Ji et al., 2014). One of the most commonly used spectral indexes is the Normalized Difference Vegetation Index (NDVI), which is defined as the difference between the Near-Infrared (NIR) and Visible (VIS, generally red) bands divided by their sum (Tucker, 1979). There has been substantial evidence that NDVI formulation can reduce atmospheric, Bidirectional Reflec-

tance Distribution Function (BRDF) and other effects (Epiphanio and Huete, 1995; Teillet et al., 1997; van Leeuwen et al., 2006).

Moderate-resolution satellite sensors provide frequent observations of the world under varying atmospheric conditions and at different observational geometries. The NDVI formulation may mitigate the abovementioned effects. In addition, compositing and noise reduction techniques are conducive to deriving temporally consistent NDVI data (Holben, 1986; Michishita et al., 2014; Maeda et al., 2016). These mathematical manipulations are generally efficient and effective for individual sensors (Yang et al., 2012; Zhang et al., 2015). However, sensor replacement and upgrading often lead to multi-sensor data discrepancies that may propagate to downstream products (Brewin et al., 2014; Pisek et al., 2015). As a result, the inter-sensor ('cross-sensor' in Volpi et al., 2015 or 'multi-sensor' in Geiß et al., 2015) band/NDVI difference has been extensively investigated among a wide variety of sensors (Trishchenko et al., 2002; Trishchenko, 2009; Gonsamo and Chen, 2013; Fan et al., 2016). These sensors include obsolete, in-orbit and planned instruments, which constitute a chronologically continuous observation system. Typical sensors include the National



* Corresponding author.

E-mail address: yb218@yahoo.com (Y. Liu).

Oceanic and Atmospheric Administration's (NOAA) Advanced Very High Resolution Radiometer (AVHRR) (Cracknell, 1997), TERRA/AQUA MODerate-resolution Imaging Spectroradiometer (MODIS) (Justice et al., 1998) and Suomi National Polar-orbiting Partnership (NPP) Visible-Infrared Imager-Radiometer Suite (VIIRS) (Cao et al., 2013). These sensors have spatial resolutions of 250–4400 m and are collectively known as moderate-resolution sensors (Trishchenko et al., 2002). Specifically, the AVHRR covers three generations of spectrally similar sensors, namely, AVHRR/1 for NOAA-8/10, AVHRR/2 for NOAA-7/9/11/12/14, and AVHRR/3 for NOAA-15 and thereafter (Trishchenko et al., 2002). These inter-sensor differences, if uncorrected, may introduce both systematic and unsystematic errors into long-term NDVI time series data (Miura et al., 2013; Tian et al., 2015).

Linear regression provides a simple method for correcting NDVI differences that is widely used at the local and regional scales (Steven et al., 2003; Thenkabail, 2004; Martínez-Beltrán et al., 2009). Miura et al. (2006) concluded that inter-sensor NDVI exhibited a nonlinear relationship. Consequently, numerous studies have used quadratic regressions to correct NDVI differences (Trishchenko et al., 2002; van Leeuwen et al., 2006; Gonsamo and Chen, 2013). However, Miura et al. (2006) proposed that the quadratic method may suffer from bias error, and the land cover dependence needed to be explicitly accounted for to reduce the error. Generally, land cover varies in space (e.g., the vegetation distribution varies with latitude and altitude) and with time (e.g., vegetation phenology). The spatio-temporal characteristics may largely complicate the patterns of inter-sensor NDVI differences, which cannot be corrected with site-independent and time-invariant methods. As a result, it is difficult to reliably use multi-sensor long-term NDVI time series data, even if the component sensor NDVI data have been accurately processed. Therefore, the dependence of the NDVI difference on land cover needs to be investigated both spatially and temporally.

Treating land cover dependency is complicated, especially when considering the atmosphere. Many studies have addressed NDVI differences in response to sensor differences due to atmospheric variations (van Leeuwen et al., 2006; Nagol et al., 2009). More studies have focused on NDVI differences resulting from sensor differences associated with land cover (Trishchenko et al., 2002; Miura et al., 2006, 2008, 2013; Trishchenko, 2009). These studies generally used twin satellite images (Rochdi and Fernandes, 2008; Li et al., 2013), hyperspectral data (Yoshioka et al., 2003; Kim et al., 2010) and simulated data (van Leeuwen et al., 2006; Gonsamo and Chen, 2013) to explore inter-sensor NDVI relationships. The satellite images, which are multispectral or hyperspectral, are confined to a specific area. Thus, the results cannot be readily transferred to other locations with different atmospheric states and surface conditions. Simulations based on canopy and radiative transfer (RT) models may disclose NDVI differences among varying sensors, over different land cover types and under different atmospheric states. However, the spatial distribution and time-varying characteristics of NDVI differences cannot be straightforwardly displayed. Therefore, a global inspection of NDVI differences among moderate-resolution sensors is needed to understand how different these NDVIs are in space and time.

To investigate inter-sensor NDVI differences among moderate-resolution sensors, state-of-the-art remote sensing derived products were used to model monthly global NDVI. These products were supported by Spectral Response Functions (SRFs) in the VIS and NIR bands of AVHRRs, MODIS and VIIRS. The multi-sensor NDVIs were compared to study spatio-temporal patterns of NDVI differences and the potential relationship with land cover. Our study furthers the understanding of global NDVI differences among multiple moderate-resolution satellite sensors, contributes to the explanation of land cover dependence of NDVI differences, and

provides recommendations for generating long-term, consistent NDVI data sets. This paper is organized as follows: Section 2 describes the data collection and processing; Section 3 states the methodologies; Section 4 presents the main results, followed by detailed discussions in Section 5; and Section 6 summarizes the major findings throughout this study.

2. Data description and processing

The objective of this section is to discuss the data collection and processing methods. Data used in this study are sensor SRFs, remote sensing derived products and spectral measurements. The major data processing schemes include spectral, spatial and temporal matching, which were used to obtain spectrally, spatially and temporally consistent data.

2.1. Spectral response functions

The moderate-resolution satellite sensors in this study include AVHRR/1 onboard NOAA-6/8/10, AVHRR/2 onboard NOAA-7/9/11/12/14, AVHRR/3 onboard NOAA-15~19/MetOp-A, MODIS and VIIRS. Fig. 1 shows the SRFs in the VIS and NIR bands. The SRFs of AVHRR/1~2 were acquired from the NOAA Polar Orbiter Data User's Guide (<http://www.ncdc.noaa.gov/oa/pod-guide/ncdc/docs/podug/html/c1/sec1-4.htm>), and those of AVHRR/3 were obtained from the NOAA KLM User's Guide (<http://www.ncdc.noaa.gov/oa/pod-guide/ncdc/docs/klm/html/d/app-d.htm>). For the two narrow-band sensors, MODIS SRFs were collected from the Ocean-Color Documents (<http://oceancolor.gsfc.nasa.gov/DOCS/RSR-tables.html>), and VIIRS SRFs were obtained from the NOAA National Calibration Center (<https://cs.star.nesdis.noaa.gov/NCC/SpectralResponseVIIRS>). MODIS sensors were onboard the TERRA and AQUA satellites, and only TERRA MODIS was selected due to data similarities. For VIIRS, the NG October 2011 band-averaged version of the SRF was used, as recommended in Moeller et al. (2011).

Fig. 1 shows the sensor SRFs, including 1a for AVHRR/1~2, 1b for AVHRR/3 and 1c for MODIS and VIIRS. With respect to AVHRR/1~2, the VIS and NIR bands overlap in the VIS-NIR transition region. The AVHRRs onboard NOAA-9/11 behave differently than other AVHRR sensors in the VIS band. The spectral responses are lower in the longer portion of the VIS spectral domain. Unlike AVHRR/1~2, no overlaps are found for AVHRR/3. Specifically, the VIS bands are narrower, and the NIR bands are flatter. Notable differences are observed in the NIR band where NOAA-18 AVHRR shows the maximum response and NOAA-19 AVHRR shows the minimum response in the longer portion of the NIR spectral domain. In contrast to the AVHRRs, MODIS and VIIRS exhibit much narrower spectral widths in both the VIS and NIR bands. These bands are less affected by atmospheric absorption.

The main preprocessing of SRF data was spectral resampling. Because the data were collected from different sources, the spectral resolutions were 2.0 nm, 1.0 nm and 0.1 nm for the AVHRR, MODIS and VIIRS spectral bands, respectively. These resolutions were resampled to 2.5 nm, as required by the Second Simulation of the Satellite Signal in the Solar Spectrum (6S) RT code (Vermote et al., 1997). The resamplings were performed using a linear interpolation method, yielding SRF data in the range of 470–1100 nm. The lower and upper limits were based on two qualifications. First, the SRF value should be less than 0.1% beyond the range of all sensors. Second, the range should be covered by the center wavelengths of the MODIS reflective solar bands (see Section 2.2).

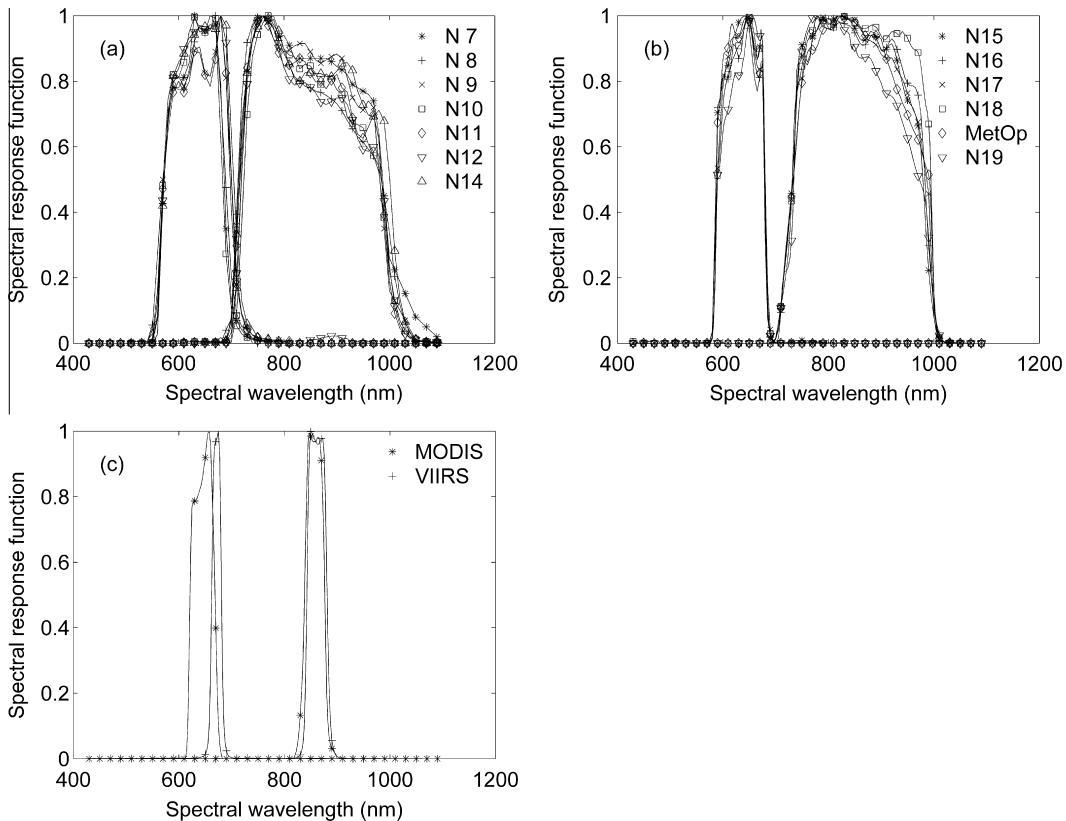


Fig. 1. Spectral response functions of (a) AVHRR/1~2, (b) AVHRR/3, and (c) MODIS and VIIRS. The data on the left denote the VIS band, and the data on the right denote the NIR band.

2.2. Remote sensing derived products

Remote sensing derived products include land surface data, atmospheric data and angular data. These products were used to model global observations and NDVIs. The land surface data include surface reflectance data, a Land Use/Land Cover (LULC) classification map and a land-sea mask. The atmospheric data consist of four atmospheric parameters, and the angular data consist of Solar Zenith Angle (SZA) and View Zenith Angle (VZA). All data were collected in 2014, except for the LULC map from 2012. Data descriptions are listed in **Table 1**. The objective of data processing is to obtain global monthly $1^\circ \times 1^\circ$ gridded parameters.

2.2.1. Land surface data

The surface reflectance data were collected from the Goddard Space Flight Center (GSFC; <https://ladsweb.nascom.nasa.gov/>). The data were $0.05^\circ \times 0.05^\circ$ MODIS Climate Modeling Grid (CMG) daily surface reflectance stored in Hierarchical Data Format (HDF). Beginning in 1998, the data were derived by correcting MODIS observations for atmospheric effects (Vermote and Vermeulen, 1999). A validation study reported better than 5% accuracy for these data (Liang et al., 2002). The five bands centered at 469 nm, 555 nm, 645 nm, 859 nm and 1240 nm were uncompressed, and the reflectance data were arithmetically aggregated into $1^\circ \times 1^\circ$ grids. The surface NDVI data were then calculated using the 645-nm (VIS) and 859-nm (NIR) bands. Subsequently, the daily NDVI data were sorted within each month to find the maximum value in each $1^\circ \times 1^\circ$ grid. The day with the maximum NDVI value was selected to represent the month. The processing method was very similar to the maximum value compositing technique (Holben, 1986), which is believed to reduce BRDF effects.

Table 1
List of remote sensing derived products.

Data	Spatial resolution	Temporal resolution	Data source
MODIS surface reflectance	$0.05^\circ \times 0.05^\circ$	Daily	GSFC
MODIS LULC	$0.05^\circ \times 0.05^\circ$	Yearly	GSFC
Land mask	$0.5^\circ \times 0.5^\circ$	Yearly	NOAA CPC
MODIS aerosol optical depth	$1^\circ \times 1^\circ$	Monthly	GSFC
MODIS solar zenith angle	$1^\circ \times 1^\circ$	Monthly	GSFC
MODIS view zenith angle	$1^\circ \times 1^\circ$	Monthly	GSFC
Aura OMI aerosol type	$0.25^\circ \times 0.25^\circ$	Daily	GES DISC
NCEP-2 water vapor	$2.5^\circ \times 2.5^\circ$	Monthly	NOAA ESRL
Aura OMI ozone	$1^\circ \times 1^\circ$	Daily	GES DISC

For each pixel, the five-band reflectance data were linearly interpolated to a 2.5 nm resolution within 470 and 1100 nm (Röder et al., 2005). Sensor-dependent surface reflectance was then calculated with the following equation (Agapiou et al., 2014; Cavalli et al., 2014):

$$\rho_s = \frac{\int SRF(\lambda)\rho(\lambda)d\lambda}{\int SRF(\lambda)d\lambda}, \quad (1)$$

where ρ_s denotes the sensor-dependent surface reflectance, SRF denotes spectral response function, ρ denotes the interpolated continuous reflectance, and λ denotes the wavelength.

With sensor-dependent surface reflectances, the Spectral Band Adjustment Factor (SBAF) can be calculated as follows (Teillet et al., 2001):

$$f = \rho'_s / \rho_s, \quad (2)$$

where f denotes SBAF for a subject relative to a reference sensor and ρ_s' and ρ_s denote the surface reflectances of the subject and reference sensors, respectively.

The LULC data were MODIS MCD12C1 (MODIS Combined Data). They were provided by GSFC as a $0.05^\circ \times 0.05^\circ$ grid in HDF format. The data used a classification tree scheme and the International Geosphere-Biosphere Program (IGBP) classification system. They were shown to be highly accurate (Friedl et al., 2002). Because the data had not been updated for 2014 at the time of this study, the latest data from 2012 were used. The assumption was that global land cover did not undergo significant changes from 2012 to 2014 at the $0.05^\circ \times 0.05^\circ$ scale. MODIS MCD12C1 included three types of land cover data, and the Major Land Cover Type 1 data with the most classes were used. The data were resampled to a $1^\circ \times 1^\circ$ grid by finding the mode value within 20×20 pixels.

The land mask data were collected from the NOAA Climate Prediction Center (CPC; ftp://cpc.ncep.noaa.gov/wd51yf/global_monthly/). The data were stored in TXT format and published as a $0.5^\circ \times 0.5^\circ$ grid. The masks were generated from typically 1-km resolution images and then spatially and temporally aggregated to $0.5^\circ \times 0.5^\circ$ monthly/yearly masks (Fan et al., 2002). Data values within 2×2 grids were averaged to obtain a $1^\circ \times 1^\circ$ global land mask map. The map described the possibility of the land being inundated, and a threshold of 50% was used to differentiate between terrestrial and oceanic areas.

2.2. Atmospheric data

The atmospheric data include Aerosol Optical Thickness (AOT) at 550 nm, aerosol type, Total Precipitable Water vapor (TPW) and Total Ozone Concentration (TOC). AOT data were obtained by MODIS MOD08 (Collection 006) and published in HDF format by GSFC. MOD08 provides monthly averaged AOT, SZA and VZA in $1^\circ \times 1^\circ$ grids. The AOT is retrieved with deep blue and dark target algorithms (Hubanks et al., 2015). A comparison with ground observations revealed an overall accuracy of 0.05 ± 0.15 for AOT (Remer et al., 2005).

Generally, aerosol is categorized into several models (types) based on its physio-chemical properties. The Aura Ozone Monitoring Instrument (OMI) OMAEROe provides daily aerosol model data. It partitions global aerosol into 4 major models and 24 minor models (http://disc.sci.gsfc.nasa.gov/Aura/data-holdings/OMI/omaero_v003.shtml). The major model includes Weakly Absorbing (WA), Carbonaceous (BB), Minerals (DD) and Volcanic Ashes (VO) (Curier et al., 2008). This approach is similar to the Continental, Biomass Burning, Desert and Stratospheric models in the 6S RT codes (Vermote et al., 1997). The daily data were distributed in $0.25^\circ \times 0.25^\circ$ grids by the Goddard Earth Sciences Data and Information Services Center (GES DISC) in NETwork Common Data Form (NETCDF) format. They were then aggregated into $1^\circ \times 1^\circ$ grids. The mode value within 4×4 grids was selected as the daily aerosol model, and the mode value within each month was selected as the monthly aerosol model.

The water vapor data were NCEP-DOE Reanalysis II (NCEP-2) monthly data in NETCDF format published by the NOAA Earth System Research Laboratory (ESRL; <http://www.esrl.noaa.gov/psd/data/gridded/data.ncep.reanalysis2.html>). The data were produced using a state-of-the-art data assimilation system and provided monthly in $2.5^\circ \times 2.5^\circ$ grids (Kanamitsu et al., 2002). The gridded data were down-scaled to $1^\circ \times 1^\circ$ grids using a cubic method. Because water vapor is continuous in space, cubic interpolation is considered reasonable (Luo et al., 2008). The ozone data were $1^\circ \times 1^\circ$ Aura OMI daily data in TXT format published by GES DISC. The data were reported to have an overall accuracy of better than 2.0% (McPeters et al., 2008). In this study, the data were arithmetically averaged within each month to generate monthly ozone data.

Satellite retrievals are generally affected by input data quality and algorithm limitations. As a result, the retrievals may be labeled as null or unreliable. For instance, MODIS surface reflectance can be obscured by clouds (Roy et al., 2006), and AOT retrieval may fail over bright surfaces (Levy et al., 2010). Moreover, SZA and VZA are also important constraints for some inversion algorithms (McPeters et al., 2008). These detrimental factors vary in space and time; therefore, monthly masks were created to mask the areas with null values or unreliable retrievals.

2.3. Spectral data

Spectral data provide better spectral resolutions and higher signal-to-noise ratios than satellite observations, benefiting model development. Because this study primarily emphasized the NDVI, only vegetation spectra were selected. The vegetation spectral data were collected from the United States Geological Survey (USGS) Digital Spectral Library (<http://speclab.cr.usgs.gov/spectral-lib.html>) (Clark et al., 1993) and Elvidge (1990). The USGS spectral data included 17 items (Fig. 2a), with spectral resolutions better than 4 nm within 200–800 nm and better than 10 nm within 800–2350 nm. Elvidge's data covered 25 green (Fig. 2b) and 74 dry (Fig. 2c) plants and were recorded every 1 nm within 400–800 nm and every 4 nm within 800–2500 nm.

The spectral data were spectrally resampled to 2.5 nm to match the spectral resolution of the SRFs. Linear interpolation was used to determine reflectance values at given wavelengths based on those at two neighboring wavelengths. Subsequently, Eq. (1) was used to calculate sensor-dependent surface reflectances, and Eq. (2) was used to obtain inter-sensor SBAFs.

3. Methodology

3.1. Determination of radiative transfer parameters

RT codes are generally used to correct satellite data for atmospheric effects and to simulate satellite data based on surface measurements. In our previous study, simplified equations were summarized for RT calculations (Fan and Liu, 2014). The radiative transfer parameters included ozone absorption, water vapor absorption, atmospheric scattering and path radiance. Detailed equations and their solutions can be found in Fan and Liu (2014).

Table 2 shows these equations. The input variables include TOC, TPW, AOT and air mass, which is approximately equal to the reciprocal of the cosine of SZA or VZA. The output variables include ozone absorption, water vapor absorption, atmospheric scattering and path radiance. The italic symbols a , b , c and d are sensor dependent coefficients. To derive these coefficients, RT codes were executed under a wide range of TOC, TPW, AOT and air mass values (Fan and Liu, 2014; Fan et al., 2015). Subsequently, the coefficients were solved under the constraint of least squares. Because our previous studies only focused on the local scale (Gobi desert in Fan and Liu, 2014) and regional scale (Yellow River Delta in Fan et al., 2015), only one aerosol model was used. Here, we incorporated the continental, biomass burning and desert models to achieve global coverage. With this method, the coefficients were determined for all the sensors in both the VIS and NIR bands and for three aerosol models.

3.2. Calculation of Top-of-Atmosphere reflectance and NDVI

With the radiative transfer parameters in Table 2 and the remote sensing derived products, the MODIS VIS/NIR band Top-of-Atmosphere (TOA) reflectances were calculated using the following equation:

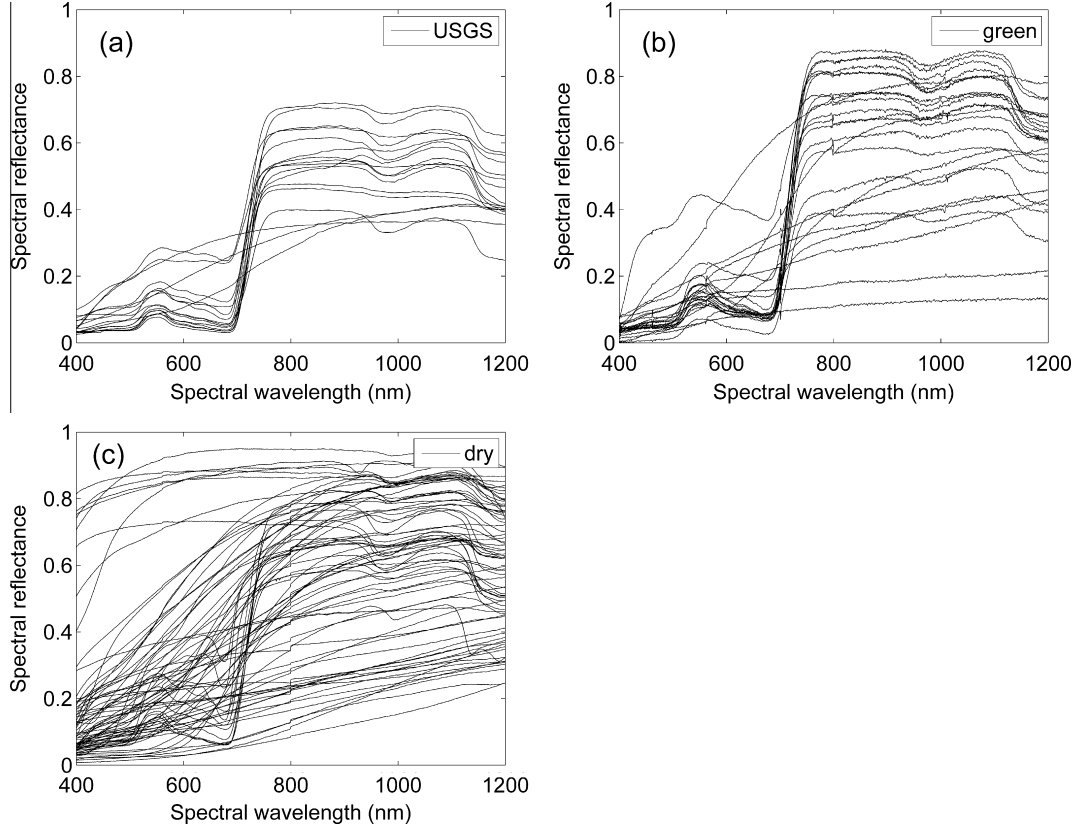


Fig. 2. Spectral data of (a) USGS vegetation, (b) Elvidge's green vegetation and (c) Elvidge's dry vegetation.

Table 2
Simplified equations for radiative transfer calculations.

Radiative var.	Equations	Input var.
Ozone absorption	$T_{g,O} = \exp(-a_1 * m * O)$	$O = \text{TOC}$
Water vapor absorption	$T_{g,W} = \exp(-\exp(b_1 + b_2 * \ln(m * W)) + b_3 * \ln^2(m * W))$	$W = \text{TPW}$
Atmospheric scattering	$T_{s(V)} = c_1 + c_2 * m * \tau + c_3/(1 + 1/m)$	$\tau = \text{AOT}$
Path radiance	$\rho_a = d_1 + d_2 * \tau$	$m = \text{air mass}$
Atmospheric albedo	$S = e_1 + e_2 * \tau + e_3 * \tau^2$	

$$\rho_{\text{TOA,MOD}} = Tg_{\text{MOD}} \left(\rho_{a,\text{MOD}} + \frac{\rho_{\text{MOD}} T s_{\text{MOD}} T v_{\text{MOD}}}{1 - \rho_{\text{MOD}} S_{\text{MOD}}} \right), \quad (3)$$

where ρ_{TOA} denotes TOA reflectance; ρ denotes surface reflectance; ρ_a denotes the path radiance; T_g denotes the total atmospheric absorption, which is approximately equal to the product of ozone and water vapor absorptions; T_s and T_v denote downwelling and upwelling atmospheric scattering, respectively; S denotes the atmospheric spherical albedo, which is strongly related to AOT; and the subscript *MOD* denotes MODIS. In this study, atmospheric spherical albedo was expressed as a quadratic function of AOT for the MODIS VIS and NIR bands (Table 2).

With MODIS TOA reflectance, TOA reflectance can be derived for other sensors in the analogous band. The formula was as follows (Fan and Liu, 2014):

$$\begin{aligned} \rho_{\text{TOA,SEN}} &= \underbrace{\frac{f T g_{\text{SEN}} T s_{\text{SEN}} T v_{\text{SEN}}}{T g_{\text{MOD}} T s_{\text{MOD}} T v_{\text{MOD}}} * \rho_{\text{TOA,MOD}}}_{\text{Multiplicative}} \\ &+ \underbrace{T g_{\text{SEN}} \left(\rho_{a,\text{SEN}} - \frac{f T s_{\text{SEN}} T v_{\text{SEN}}}{T s_{\text{MOD}} T v_{\text{MOD}}} \rho_{a,\text{MOD}} \right)}_{\text{Additive}} \end{aligned} \quad (4)$$

where f denotes the SBAF relative to MODIS and the subscript *SEN* denotes any sensor except for MODIS. Definitions of other variables are the same as those in Eq. (3).

With the TOA reflectances, NDVI was calculated as follows:

$$\text{NDVI} = \frac{\rho_{\text{TOA,NIR}} - \rho_{\text{TOA,VIS}}}{\rho_{\text{TOA,NIR}} + \rho_{\text{TOA,VIS}}}, \quad (5)$$

where subscripts *VIS* and *NIR* denote the VIS and NIR bands, respectively.

3.3. Dual-sensor NDVI difference and its relationship with LULC

With Eq. (5), the NDVI difference was calculated as follows:

$$\Delta \text{NDVI} = \text{NDVI}_s - \text{NDVI}_r, \quad (6)$$

where ΔNDVI denotes the NDVI difference and NDVI_s and NDVI_r denote NDVIs from the subject and reference sensors, respectively.

The NDVI difference was visually inspected to determine its spatial distribution. Furthermore, monthly histograms were compared to investigate the potential dependence of the NDVI difference on LULC type. The selected months were January and July, which are representative of the Northern Hemisphere winter and summer seasons. In a quantitative manner, the NDVI difference was regressed using the subject sensor NDVI for each month. The regression equation is as follows:

$$\Delta \text{NDVI}_{\text{LULC},T} = a_{\text{LULC},T} * \text{NDVI}_{s,\text{LULC},T} + b_{\text{LULC},T}, \quad (7)$$

where the coefficients $a_{\text{LULC},T}$ and $b_{\text{LULC},T}$ denote the LULC-dependent and time (*T*)-varying regression coefficients, respectively.

The monthly variation in $a_{\text{LULC},T}$ was investigated for different LULC types to determine how land cover affected inter-sensor

NDVI transformations and how the transformations varied with time.

3.4. Determination of reference sensor(s) for NDVI comparison

Statistical analysis was used to determine sensor(s) to which other sensors were referenced. For the sensor-dependent surface reflectances and NDVIs in Section 2.3, the following equations were developed:

$$\rho_i = a_\rho * \rho_{j,j \neq i} + b_\rho \quad \text{and} \quad (8)$$

$$NDVI_i = a_{NDVI} * NDVI_{j,j \neq i} + b_{NDVI}, \quad (9)$$

where ρ and $NDVI$ denote surface reflectance and NDVI, respectively; i denotes the candidate reference sensor; j denotes the non-candidate sensors; and a_ρ , b_ρ , a_{NDVI} and b_{NDVI} are regression coefficients.

To evaluate the performances of Eqs. (8) and (9), the following metrics were used:

$$R^2 = 1 - \frac{\sum (\hat{y}_i - y_i)^2}{\sum (y_i - \bar{y})^2} \quad (10)$$

$$RMSE = \left[\frac{\sum (\hat{y}_i - y_i)^2}{N} \right]^{1/2} \quad (11)$$

where R^2 is the coefficient of determination, $RMSE$ is the root mean square error, y denotes the dependent variable with a mean value of \bar{y} , \hat{y} denotes the estimated value, and N denotes the number of samples.

In this study, the optimal reference sensor(s) were determined as having close-to-unity slope values in Eqs. (8) and (9).

4. Results

4.1. Global distributions of atmospheric, angular and surface parameters

Figs. 3 and 4 show the global distributions of atmospheric, angular and surface parameters in January and July, which are representative of the Northern Hemisphere winter and summer seasons. In general, TOC increases from the equator toward Polar Regions, and it exhibits an overall increase from January to July. Most water vapor is located between 30°S and 30°N and shifts toward the Northern Hemisphere in July. AOT is stable and well below 1.0 throughout the year. However, the aerosol model varies, with more biomass burning aerosol in July in both hemispheres. In January, SZA is higher over the Northern Hemisphere, whereas in July, it is higher over the Southern Hemisphere. The VZA generally falls between 30° and 45° and increases from low-latitude to high-latitude areas.

The VIS band surface reflectance is higher in the North African deserts and lower for other terrestrial surfaces. However, the NIR band reflectance is not as distinct as the VIS band reflectance. A large portion of vegetated land shows reflectance values similar to those in desert areas. Due to vegetation phenology, the NIR band surface reflectance is brighter over the Northern Hemisphere in July than in January. Vegetation green-up is also observed with the NDVI increase in July. Notably, NDVI values in the desert areas remain almost unchanged in the two months.

Fig. 5 shows the global distribution of LULC type at a $1^\circ \times 1^\circ$ resolution. Approximately one third of the Earth's surface (33.1%) is covered by snow and ice, followed by open shrubland (14.0%) and grassland (10.3%). Snow and ice are mostly distributed in the Antarctic. A total of 74.1% of open shrublands and 89.4% of grass-

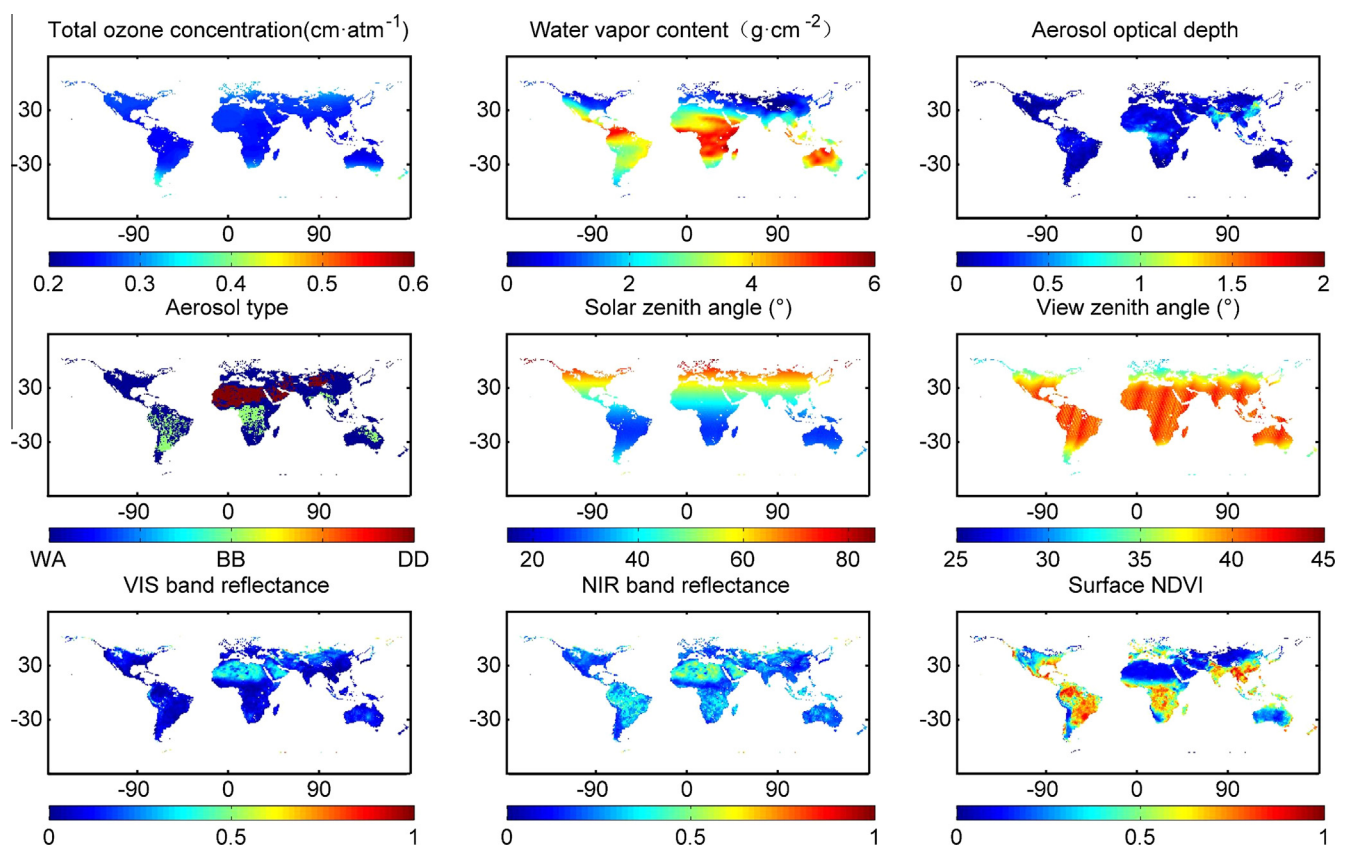


Fig. 3. Global distributions of atmospheric, angular and surface parameters in January.

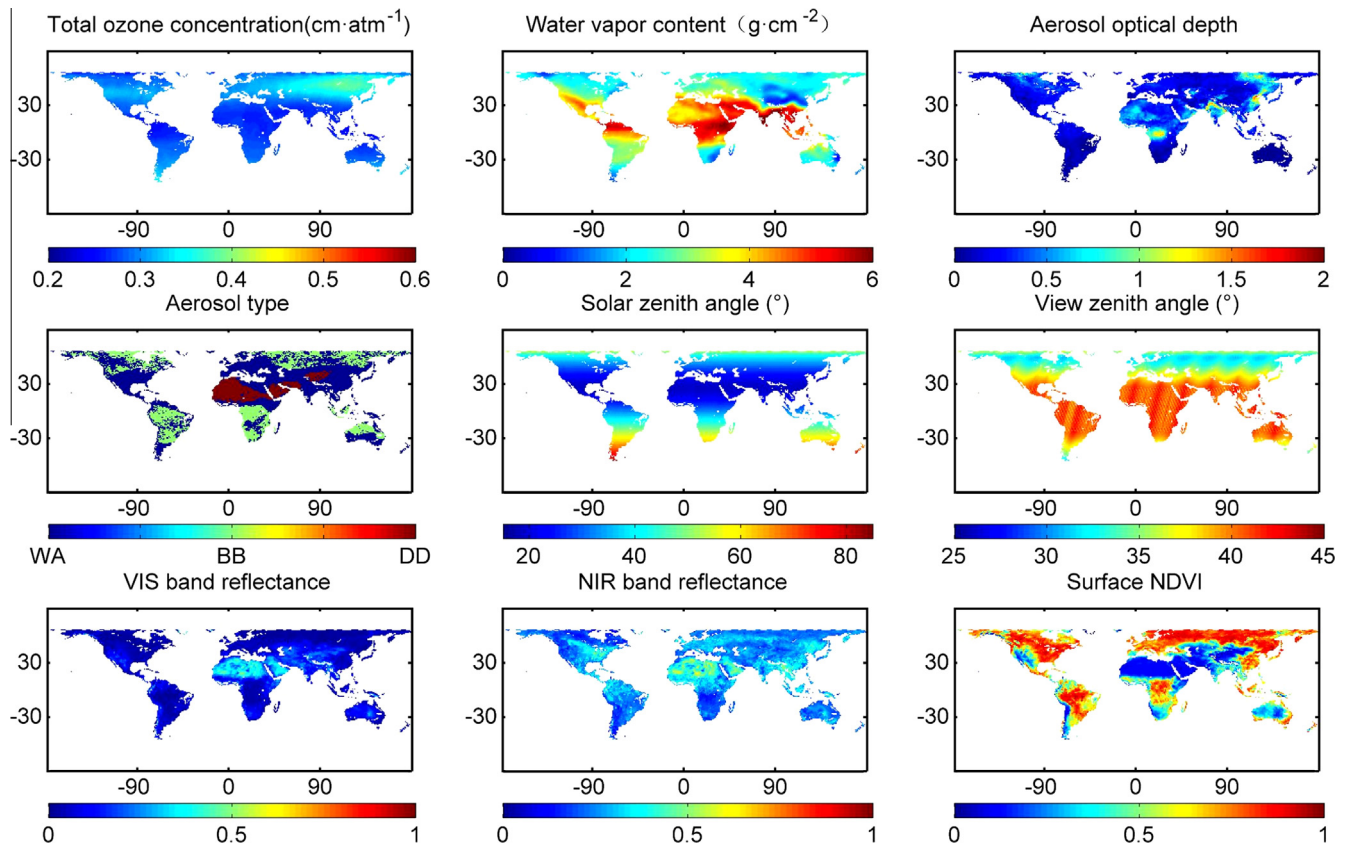


Fig. 4. Global distributions of atmospheric, angular and surface parameters in July.

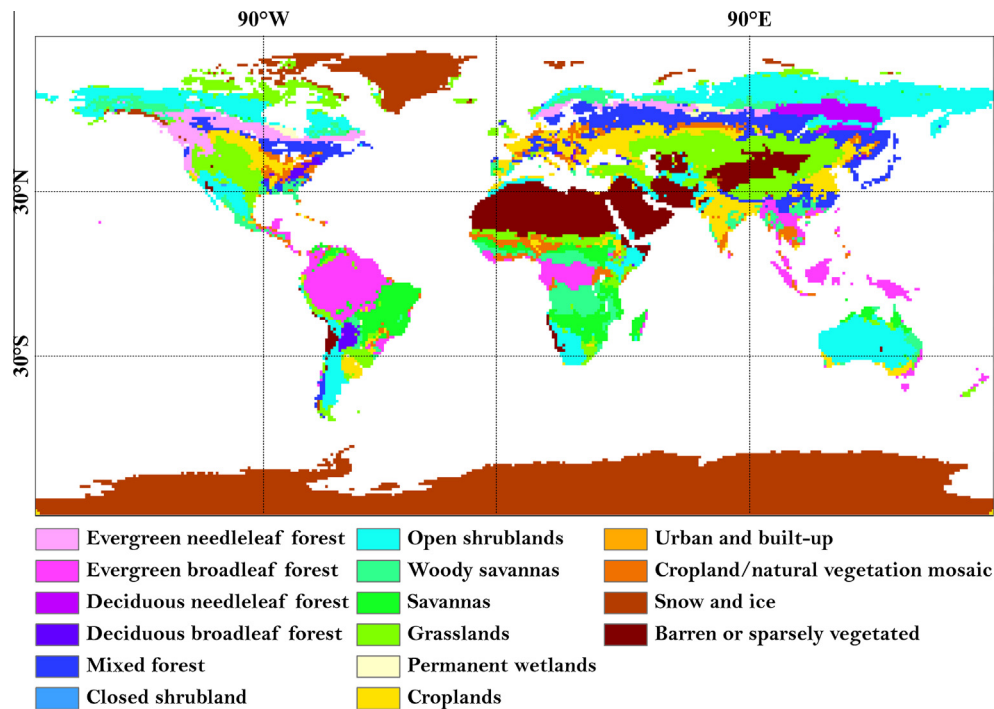


Fig. 5. $1^\circ \times 1^\circ$ global LULC map.

lands are located in the Northern Hemisphere. The other dominant LULC types are barren or sparsely vegetated land (8.4%), mixed forest (6.2%), cropland (5.9%), evergreen broadleaf forest (5.5%), woody savannas (5.0%) and savannas (3.9%). The barren or sparsely

vegetated land is dominated by deserts in North Africa and China near 30°N . Mixed forests are mostly distributed near approximately 50°N and in South China. Most cropland and woody savanna areas are also spread over the Northern Hemisphere. Ever-

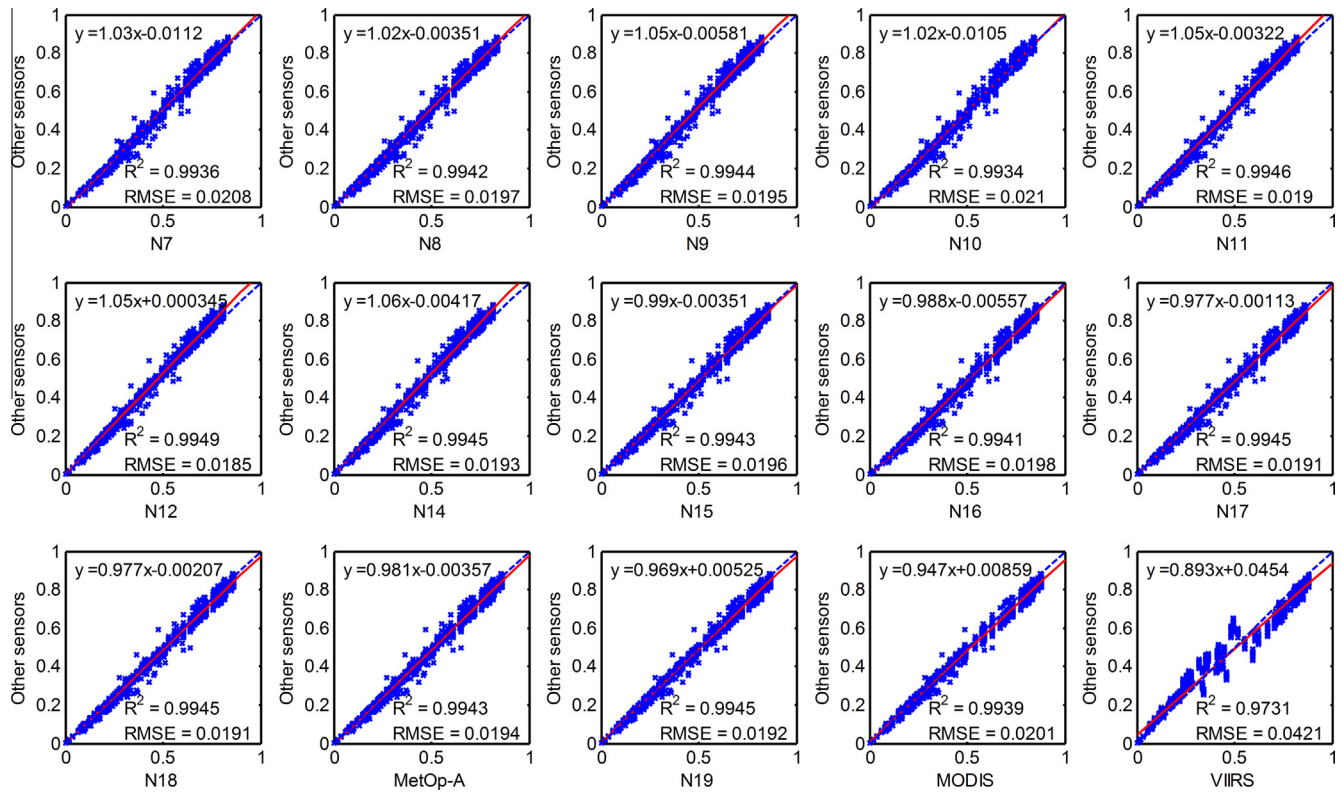


Fig. 6. Comparisons between the surface reflectances of the candidate reference sensor and other sensors in the VIS band. The horizontal axis denotes the candidate reference sensor, and the vertical axis denotes other sensors.

green broadleaf forests and savannas are only located near the equator. In addition, permanent wetlands and urban/built-up lands are mostly in the Northern Hemisphere. Both evergreen and deciduous forests grow in remote areas of the Northern Hemisphere. In general, most of the land cover types are associated with the Northern Hemisphere.

4.2. The reference sensor(s) for NDVI comparison

Fig. 6 shows a comparison between the surface reflectances of a candidate reference sensor and other sensors in the VIS band. The horizontal axis denotes the candidate reference sensor, and the vertical axis denotes the other sensors. A linear regression shows that all the AVHRR/1~2 sensors have slope values of 1.01. For AVHRR/3, the NOAA-15~16 AVHRRs have slope values of 1.00, and the other sensors have values less than 1.00. The slope values are 0.976 for MODIS and 0.933 for VIIRS. Fig. 7 shows the same comparison but for the NIR band. The slope values are 1.01 for AVHRR/1~2, except for NOAA-10 AVHRR (slope = 1.00), and are less than 1.00 for AVHRR/3, except for NOAA-18 AVHRR (slope = 1.00). Similar to the VIS band, MODIS and VIIRS also have smaller slope values (0.971 and 0.973) in the NIR band. Overall, the modern sensors generally observe high surface reflectance in both the VIS and NIR bands.

Fig. 8 shows a comparison between the NDVIs of the candidate reference sensor and other sensors. The slope values are generally higher than unity (1.02–1.06) for AVHRR/1~2 and less than or equal to 0.99 for AVHRR/3. Notably, the slope values are 0.947 for MODIS and 0.893 for VIIRS. The implication is that modern sensors tend to have higher NDVI values, which is favorable to overcoming atmospheric effects. Note that NOAA-15~16 AVHRRs are associated with close-to-unity slope values. The slope values are 0.990 for NOAA 15 and 0.988 for NOAA 16. Correspondingly,

slope values are both 1.00 for the VIS band (Fig. 6) and 0.998 & 0.999 for the NIR band (Fig. 7). The NOAA-15~16 AVHRRs exhibit an overall smaller difference than do the other sensors for both reflectance and NDVI. Therefore, NOAA-15 in the A.M. orbit and NOAA-16 in the P.M. orbit are selected as reference sensors. Because the two sensors share similar SRFs, only NOAA 15 AVHRR is considered hereinafter.

4.3. General patterns of NDVI differences

Fig. 9 illustrates the global NDVI difference for moderate-resolution sensors relative to NOAA-15 AVHRR in January. With respect to AVHRR/1~2, the NDVI difference is generally negative. Notable difference can be seen in parts of South America, South Africa and South Asia. Within AVHRR/1~2, NOAA-7/8/10 AVHRRs show similar spatial patterns, and NOAA-9/11/12/14 AVHRRs also show similarities. Unlike AVHRR/1~2, the AVHRR/3 NDVIs are very close to the NOAA-15 NDVI. The NDVI difference is globally below 0.1 NDVI units for terrestrial surfaces. Contrary to the AVHRR sensor values, MODIS and VIIRS show positive NDVI differences in most regions. The MODIS NDVI has an overall positive bias of up to 0.15 NDVI units, whereas the VIIRS NDVI exhibits a mixed pattern of biases. The bias varies from low values in regions beyond 30°N to high values in Central Africa.

Fig. 10 illustrates the NDVI difference in July. The spatial patterns of NDVI difference are very similar to those in January, yet the overall difference is intensified. In addition, the regions with large NDVI differences generally shift toward the Northern Hemisphere in July. The shift in the NDVI difference is in good agreement with vegetation green-up and growth in July in the Northern Hemisphere. Notably, the regions beyond 30°N appear to have large negative NDVI biases for AVHRR/1~2 in July. However, these regions are masked in January because of large SZAs.

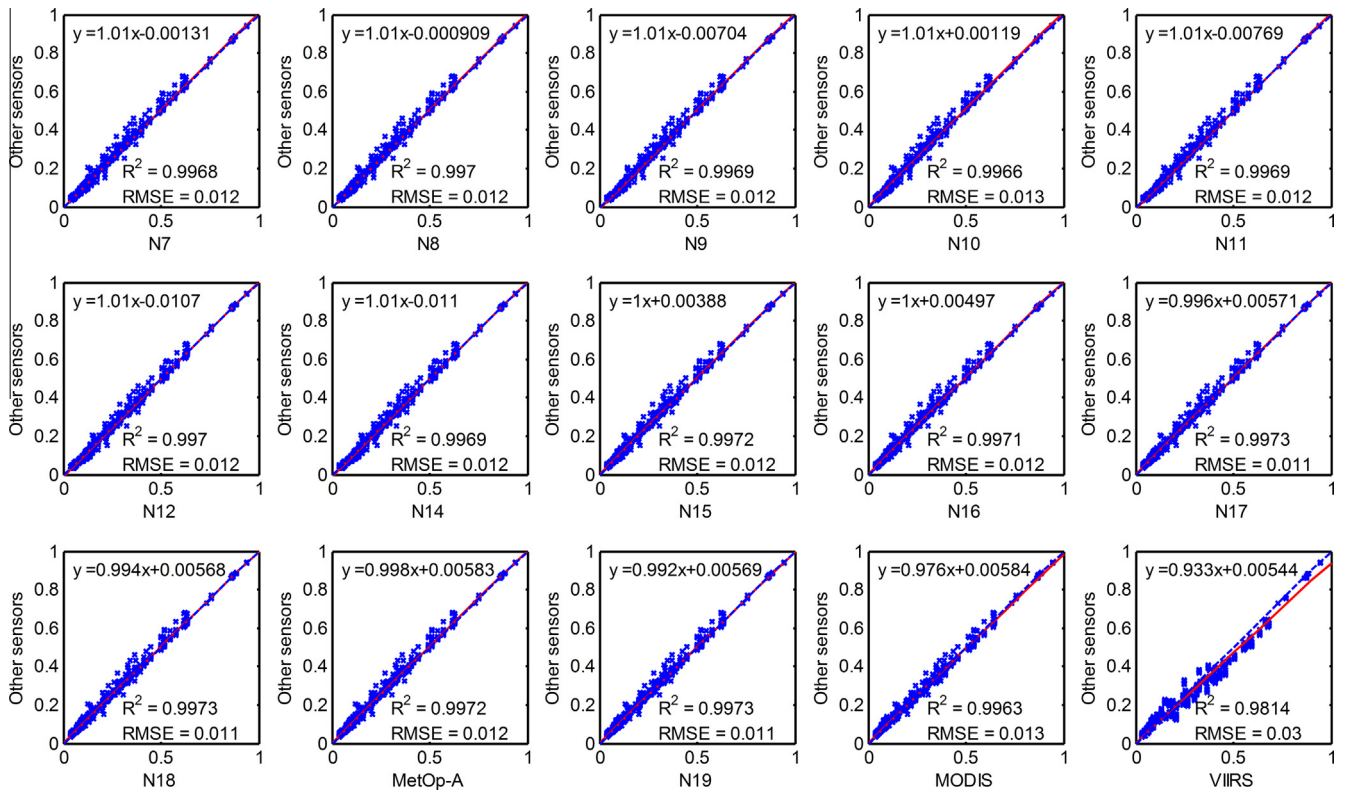


Fig. 7. Comparisons between the surface reflectances of the candidate reference sensor and other sensors in the NIR band. The horizontal axis denotes the candidate reference sensor, and the vertical axis denotes other sensors.

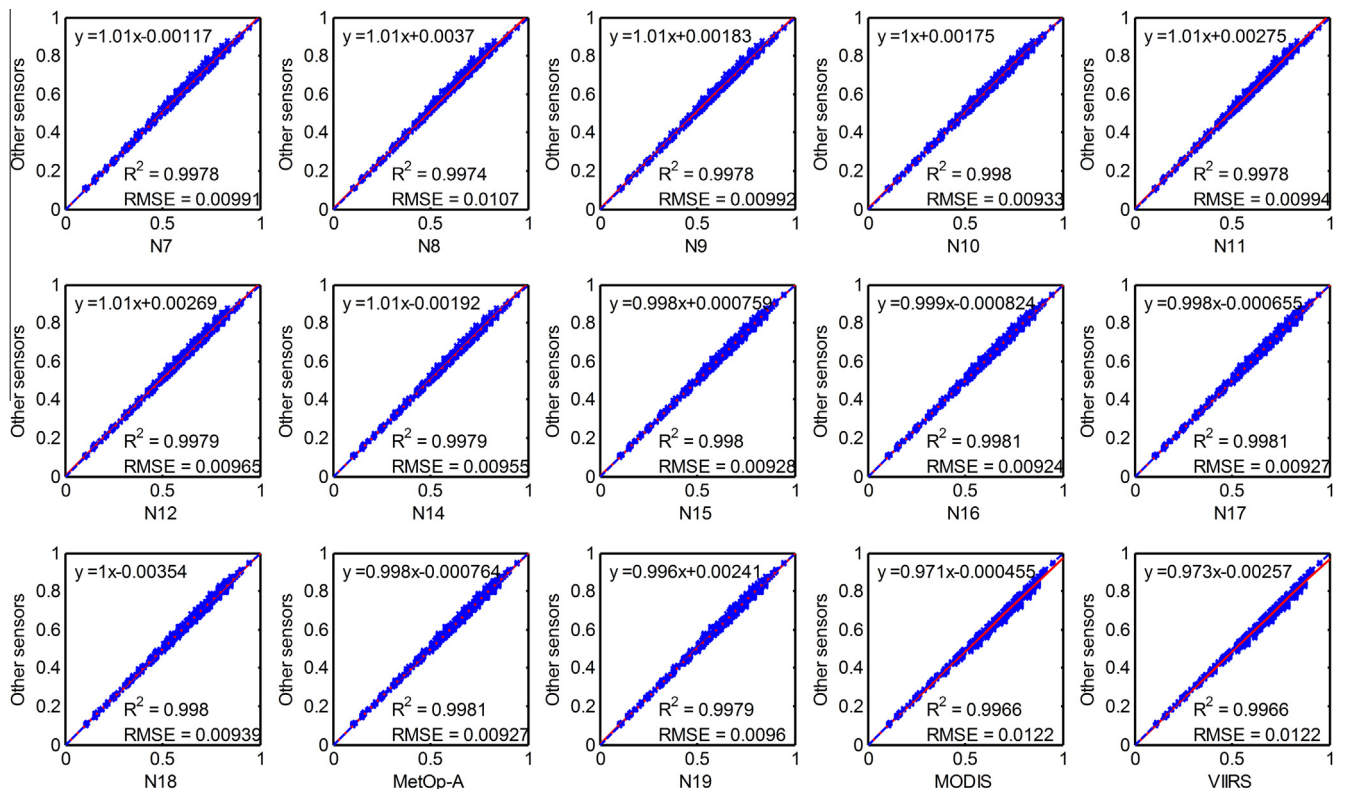


Fig. 8. Comparisons between the NDVIs of the candidate reference sensor and those of other sensors. The horizontal axis denotes the candidate reference sensor, and the vertical axis denotes other sensors.

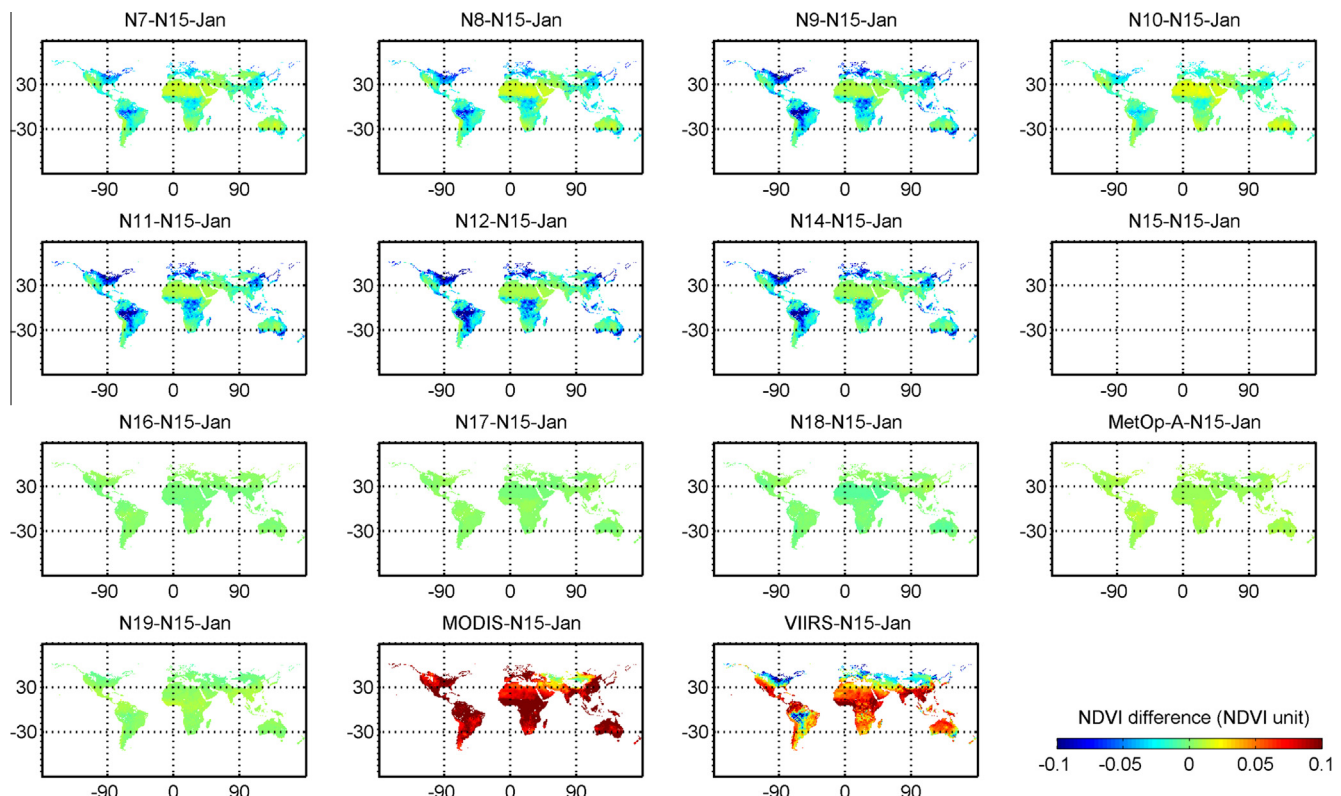


Fig. 9. Global NDVI difference relative to NOAA-15 AVHRR in January.

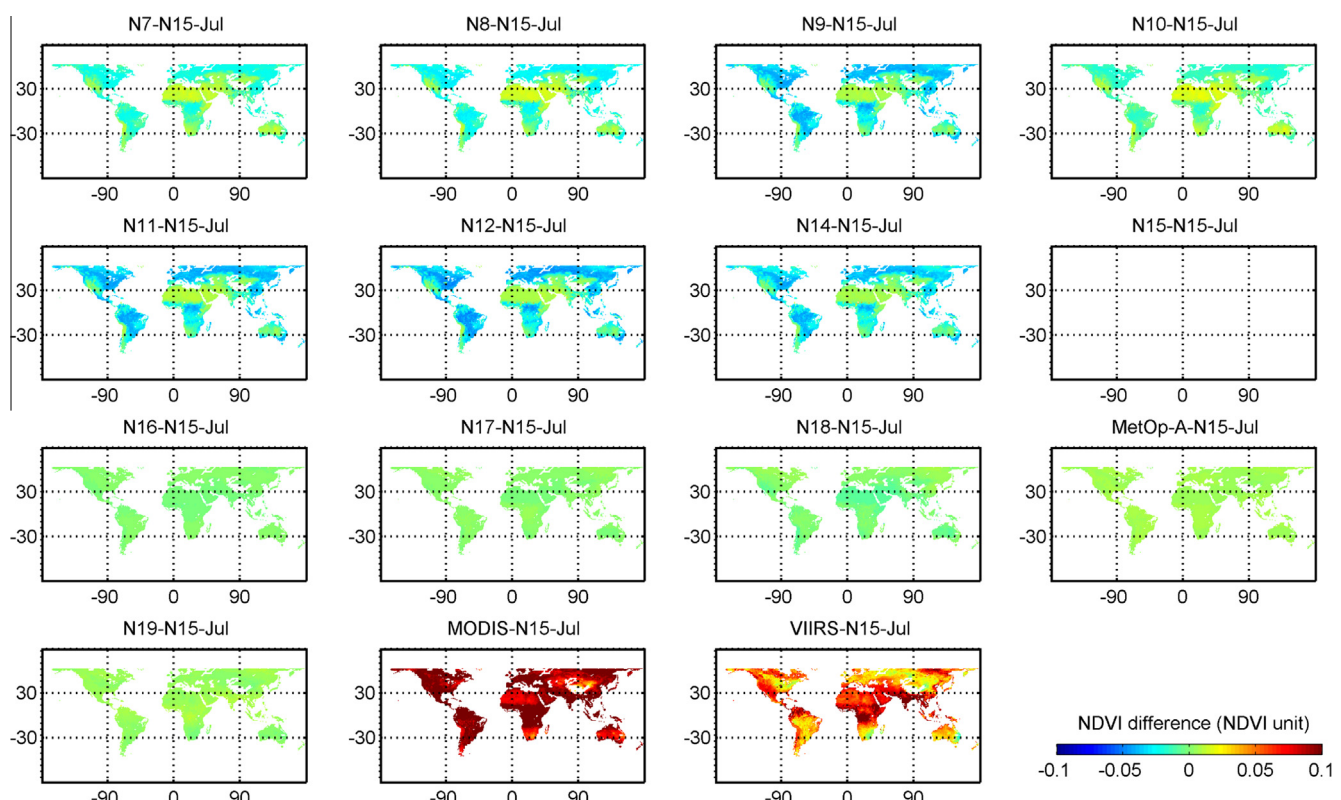


Fig. 10. Global NDVI difference relative to NOAA-15 AVHRR in July.

Similar to that in January, the NDVI difference is negligibly small for AVHRR/3 throughout the world. For the two modern sensors,

MODIS still shows an overall positive bias, and VIIRS shows mixed NDVI differences.

4.4. Dependence of the NDVI difference on LULC

Fig. 11 illustrates histograms of the NDVI difference (NOAA-7 – NOAA-15) for individual LULC types in January. **Fig. 12** shows the histograms in July. NOAA-7 is selected to represent AVHRR/2, with NOAA-15 as the reference. For evergreen broadleaf forest in January, the NDVI difference is primarily negative, with a peak value at ~ -0.023 . The frequency distribution remains almost unchanged in July, and the peak value is ~ -0.024 . Because evergreen broadleaf forest undergoes little seasonal change, this demonstrates that the atmosphere plays a minor role in the NDVI difference. For deciduous broadleaf forest in January, the NDVI difference exhibits two peaks centered at ~ -0.025 and ~ -0.006 . In July, however, the NDVI difference is concentrated within a narrow range centered at ~ -0.024 . Regeneration of leaves may be the cause of this distribution change. On a global scale, the histogram and its seasonal differences can be determined by latitude difference and vegetation phenology for vegetated land cover types.

The NDVI difference over mixed forest shows an approximately uniform distribution in January, whereas it is highly concentrated around ~ -0.025 in July. Closed shrubland covers only four $1^\circ \times 1^\circ$ grids, and its NDVI difference is close to zero for both months. Snow and ice also shows a similar pattern and is one of the LULC types with the smallest NDVI difference. It is likely attributable to the relatively flatter spectral curves in the VIS-NIR bands. Open shrubland exhibits a different pattern than does closed shrubland. The majority of open shrubland has a positive NDVI bias in January, but a new peak value centered at ~ -0.020 appears in July. The difference is well below zero for woody savannas, which show subtle changes from January to July. The distribution shifts slightly in the negative direction. Conversely, the distribution peaks at ~ -0.024 in January in savannas and shows a quasi-uniform distribution between ~ -0.024 and ~ 0.008 in July.

Grassland and cropland are common LULC types in the Northern Hemisphere. The distribution peaks at ~ 0.004 for grassland in January, but shows a quasi-uniform distribution between ~ -0.025 and ~ 0.008 in July. Cropland in winter has an NDVI differ-

ence between ~ -0.025 and ~ 0.010 . However, the difference in summer shows a distribution with a narrow and steep peak at ~ -0.025 and a broad and gentle plateau between ~ -0.020 and ~ 0.006 . This distribution also applies to cropland/natural vegetation mosaics and even permanent wetlands.

Only two urban and built-up grids in the Northern Hemisphere are visible on the $1^\circ \times 1^\circ$ LULC map. The NDVI difference is $-0.005/-0.010$ in January and $-0.020/-0.025$ in July. Because atmospheric effects have been demonstrated as negligible, the inter-month differences may be attributable to vegetation growth in the Northern Hemisphere during the summer. Unlike the values in vegetated regions, barren or sparsely vegetated regions have NDVI differences greater than zero. The peak value is ~ 0.012 in both months. The lower part of the NDVI difference shifts slightly in the negative direction, likely resulting from vegetation growth.

4.5. Seasonal variation in the relationship between NDVI and NDVI difference

Fig. 13 shows the slopes of NDVI difference vs. subject NDVI for typical land cover types. The land cover types include evergreen broadleaf forest, mixed forest, woody savannas, grasslands, croplands and croplands/natural vegetation mosaics. The first three land cover types generally undergo little seasonal changes, whereas the remaining types have significant phenological changes. In **Fig. 13**, the horizontal axis represents the month, and the vertical axis represents the slope value. The slope values are stable at the monthly scale (vary by $\leq 10^{-4}$ NDVI units per month) for the first three land cover types and vary significantly for the other land cover types. With respect to grasslands, the slope value has a unimodal distribution, with a peak value in June/July. The croplands and croplands/natural vegetation mosaics, however, exhibit bimodal distributions. The peak values appear in April and September/October for croplands and in April and October/November for croplands/natural vegetation mosaics. The red curves represent the sixth-order fitting line, which is used to find the months with peak values. In general, April and October are typ-

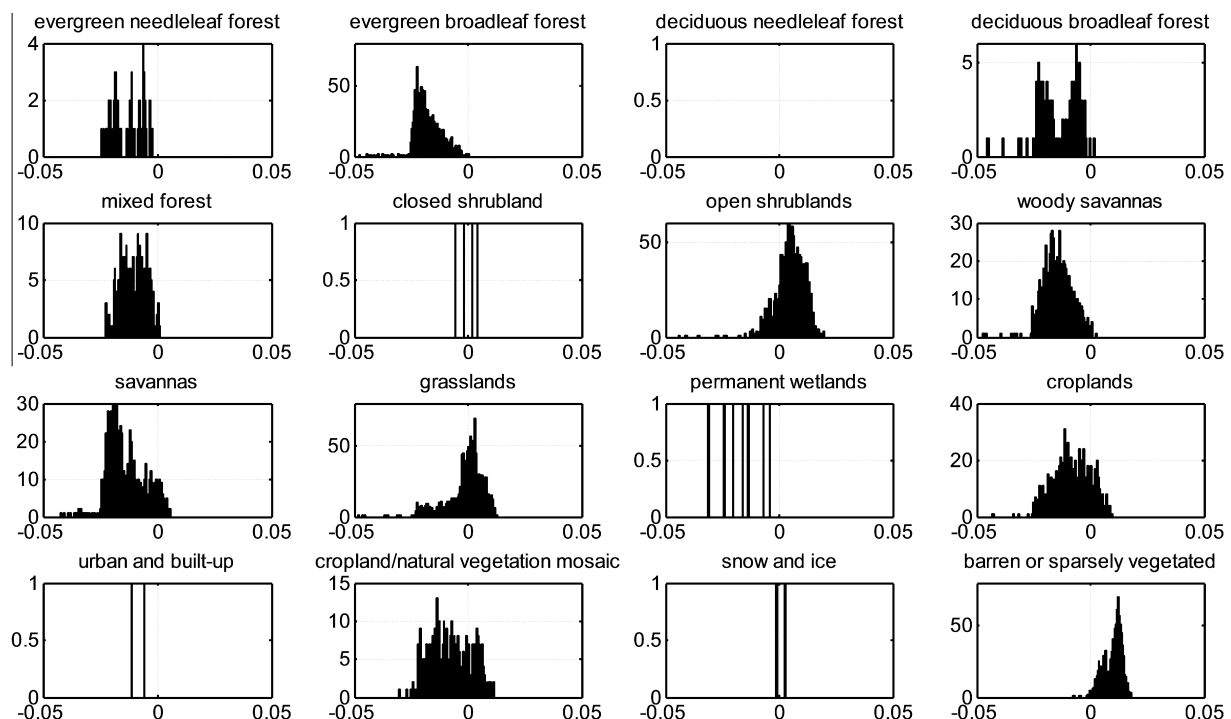


Fig. 11. Histograms of the AVHRR NDVI difference (NOAA-7 – NOAA-15) for various LULC types in January.

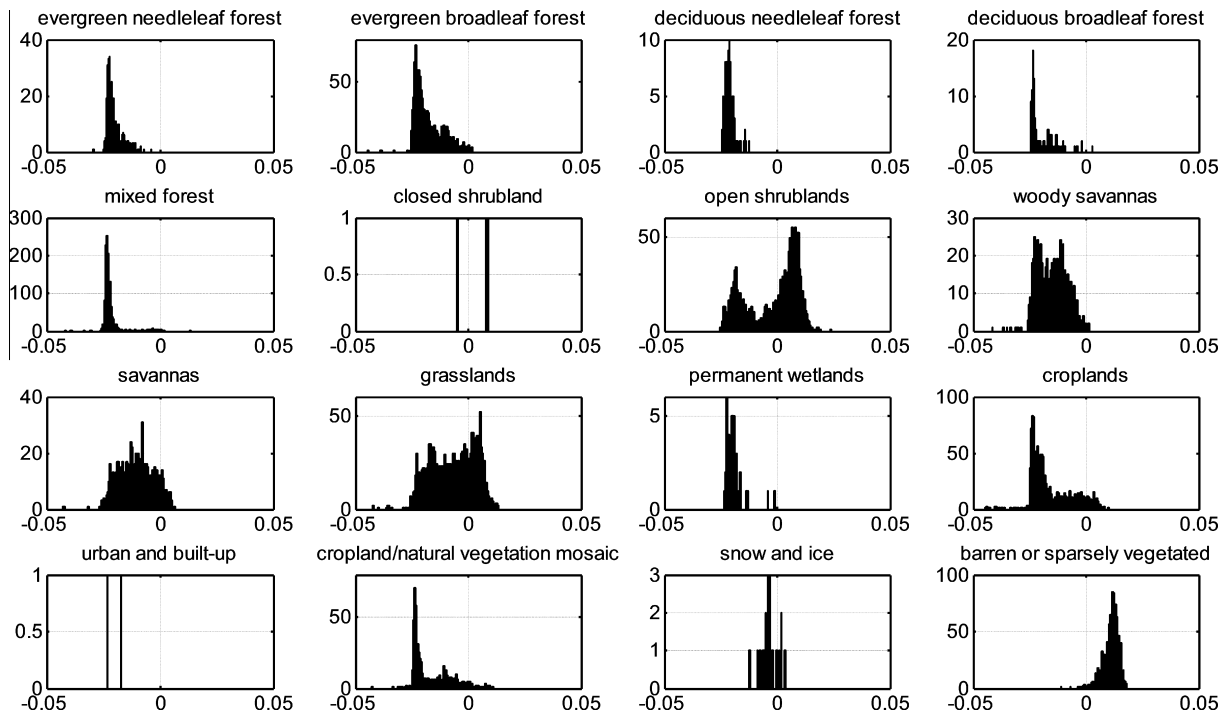


Fig. 12. Histograms of the AVHRR NDVI difference (NOAA-7 – NOAA-15) for various LULC types in July.

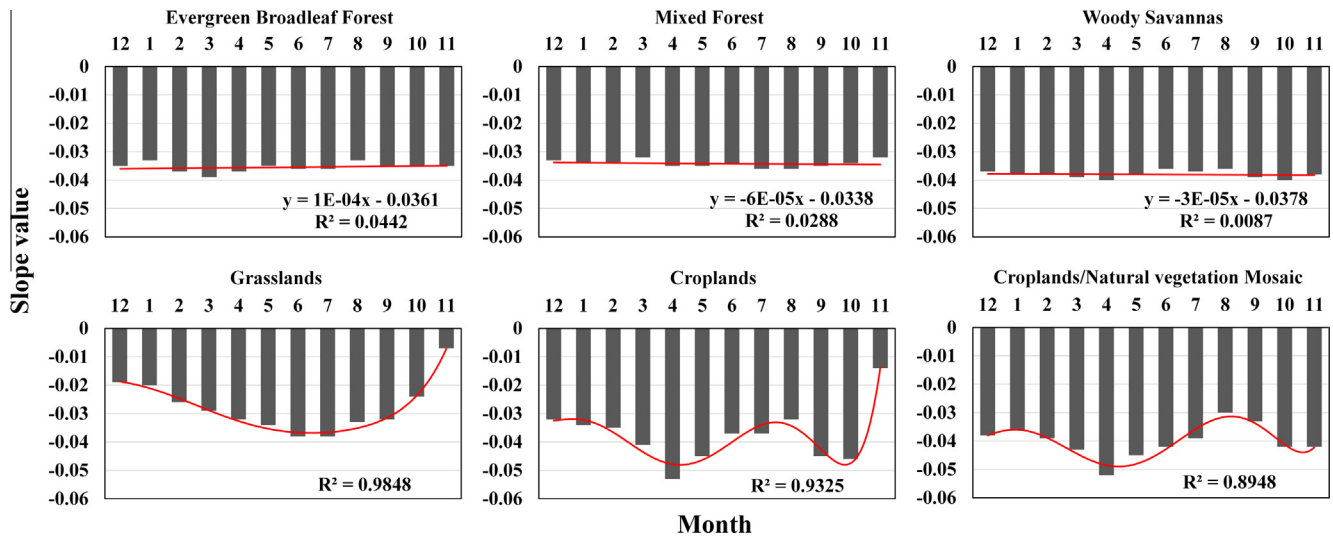


Fig. 13. Seasonal variations in the slope value in Eq. (7) for evergreen broadleaf forest, mixed forest, woody savannas, grasslands, croplands and croplands/natural vegetation mosaics.

ical harvesting times in the Southern and Northern Hemispheres. Croplands reach maturity in these months and are harvested thereafter. Most grasses grow in the Northern Hemisphere without disturbance (such as harvesting); therefore, the NDVI difference shows a unimodal distribution.

5. Discussion

5.1. The reasonability of NOAA 15~16 AVHRRs as reference sensors

Figs. 6–8 show the potential of NOAA-15~16 AVHRRs as reference sensors for multi-sensor NDVI comparison. Ideally, NOAA-15 AVHRR can be used as reference for sensors in the A.M. orbit, and NOAA-16 AVHRR can be used for sensors in the P.M. orbit. Spec-

trally, these sensors provide benchmarks that connect the preceding sensors and succeeding sensors. Scientific and technological developments have gradually improved sensor performance. As a result, the sensors have progressively smaller overlapping areas in the VIS-NIR transition region from AVHRR/1~2 to AVHRR/3 and finally to MODIS and VIIRS (Gonsamo and Chen, 2013). In this sense, the intermediate AVHRR/3 sensors are ideal candidate references for sensor comparisons. As early representatives of AVHRR/3, NOAA-15/16 AVHRRs spectrally resemble AVHRR/1~2 and match other AVHRR/3 sensors. Therefore, the twin sensors are selected to minimize the overall difference among moderate-resolution sensors.

Some might suggest that MODIS is a more suitable reference sensor. TERRA and AQUA MODIS provide state-of-the-art NDVI

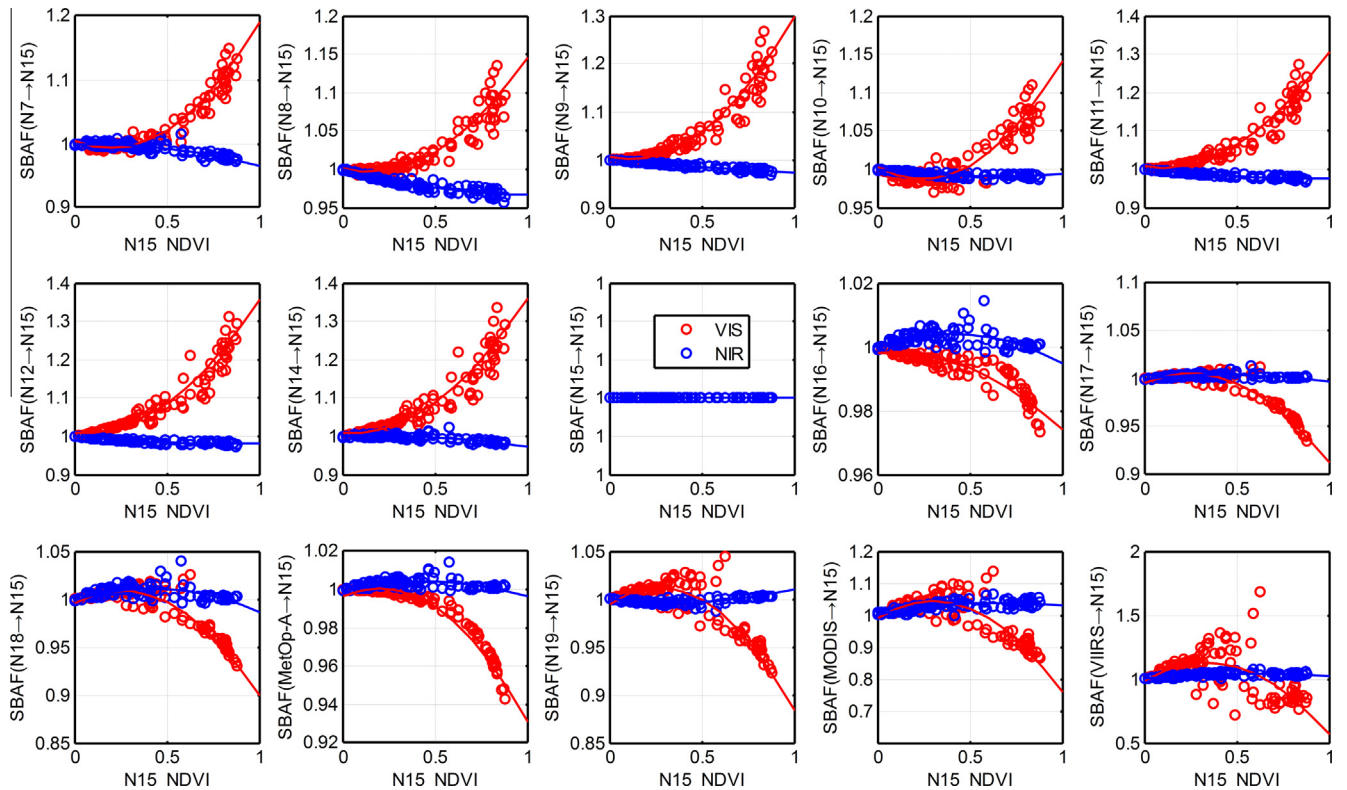


Fig. 14. Relationship between spectral band adjustment factors in the VIS/NIR bands and NDVI.

products, offering data that are more atmosphere resistant and sensitive than AVHRR data. However, the NDVI difference is significant between MODIS and AVHRR at both top-of-canopy (Fig. 8) and top-of-atmosphere levels (Figs. 9 and 10). Additionally, the MODIS-AVHRR difference exhibits a complicated spatial distribution (Figs. 9 and 10) that is difficult to correct. Likely due to the considerable difference in the VIS band (Fig. 1), VIIRS-AVHRR NDVI shows an even more complicated spatial variability, and the pattern of variability also varies with time (Figs. 9 and 10). Because a variety of AVHRR sensors are currently in operation and new sensors such as MetOp-B AVHRR have been launched, a mere combination of AVHRRs may meet the demands of the scientific community. For instance, the release of Global Inventory Modeling and Mapping Studies (GIMMS) NDVI_{3g} has attracted a wide range of users (Zhu et al., 2013; Pinzon and Tucker, 2014).

5.2. Explanation of the relationship between NDVI difference and NDVI

Our study reveals a general rule that the NDVI difference increases with NDVI for AVHRR/1~2 referenced to AVHRR/3. The conclusion is verified by visual inspection (Section 4.3), histogram comparisons (Section 4.4) and statistical regression (Section 4.5). The positive relationship is also the underlying reason why a number of studies use linear regression to intercalibrate multi-sensor NDVI data. With a general NDVI intercalibration equation of $NDVI_2 = a * NDVI_1 + b$, one can easily derive another equation $NDVI_2 - NDVI_1 = (a - 1) * NDVI_1 + b$. In the Results section, $NDVI_1$ and $NDVI_2$ represent NOAA-15 AVHRR NDVI and NOAA-7 AVHRR NDVI, respectively, and the coefficient a is greater than unity for most vegetated land cover types. Therefore, the NDVI difference increases with NDVI itself.

The atmosphere plays a minor role in the NDVI difference (evergreen broadleaf forest and barren/sparsely vegetated regions in Figs. 9 and 10); therefore, land cover should be the major contrib-

utor. To understand the positive correlation between the NDVI difference and NDVI, SBAFs (referenced to NOAA-15 AVHRR) in both the VIS and NIR bands are plotted as functions of NDVI. Fig. 14 shows a strong quadratic relationship between the VIS band SBAF and NDVI. The data used are the same as those in Figs. 6–8. The SBAF increases with NDVI for AVHRR/1~2 and decreases for AVHRR/3. Unlike the VIS band SBAF, the NIR band SBAF varies slightly with NDVI. As a result, the difference increases with NDVI in the VIS band and remains relatively stable in the NIR band. Therefore, the NDVI difference increases with NDVI. Note that the regression is not good for VIIRS. This may be the cause of different VIIRS-AVHRR NDVI difference patterns in Figs. 10 and 11.

5.3. Comparison with previous studies

The object of our study is to understand the potential land cover dependency on NDVI consistency. Trishchenko et al. (2002) and Miura et al. (2013) found that the NDVI difference between AVHRR/3 and AVHRR/1~2 increases with NDVI; however, they did not investigate the underlying reasons. In addition, Miura et al. (2013) reported both systematic and unsystematic differences between VIIRS and AVHRR/3 NDVI, but their study only concentrated on 13 land cover types and showed no global distribution of NDVI differences. The land cover types in Miura et al. (2006) only included sandy beach, burned savanna, savanna grassland, riparian forest, primary forest and cultivated pasture. Our study, however, is based on global surface reflectance data and atmospheric data. The primary results promote our understanding of the NDVI difference in the context of global coverage.

For the first time, this study considers seasonal changes in NDVI intercalibration. In our study, the seasonal changes include both surface changes and atmospheric variations. Twelve months of composite surface reflectance and atmospheric data are used instead of model simulations based on assumed surface conditions

and atmospheric states. Accounting for the time-dependent NDVI intercalibration is of vital importance, especially for land cover types undergoing significant phenological changes. Our study also has important implications for generating long-term NDVI data sets. According to our findings, significant NDVI differences can still exist among sensors, although compositing techniques may largely reduce the atmospheric and BRDF effects of individual sensors. Therefore, it is recommended that land cover-dependent and seasonally varying intercalibration equations be used to correct these differences. Because this study is based on simulations without regard to the spatial resolutions of sensors, future attention should be paid to the impacts of pixel size differences (Curran and Williamson, 1986).

6. Conclusions

Moderate-resolution satellite sensors have provided substantial scientific data for monitoring environmental changes. Deriving multi-sensor NDVI consistently is an indispensable technological process associated with the reliable use of these data. In this context, a simulation study is performed to investigate the land cover dependency of the NDVI difference and determine the underlying reasons. The simulation is based on radiative transfer calculations that are supported by monthly global land surface, atmospheric and sensor geometry data. Because our study first models sensor spectral bands and then combines the bands into a spectral index, it can be easily adapted to other spectral indices.

Our study reveals that land cover differences and not atmospheric variations are the main factors that account for NDVI differences among different generations of AVHRR. Relative to NOAA-15 AVHRR, the NDVI difference shows a distinct global pattern for AVHRR/1~2, with considerable negative differences in highly vegetated areas and subtle positive differences in non-vegetated or sparsely vegetated areas. The negative NDVI bias shifts northward in the Northern Hemisphere during the summer. For land cover types that undergo minor phenological changes, the NDVI intercalibration equation remains stable throughout the year. However, the equation varies significantly for land cover types that undergo significant phenological changes.

The positive relationship between the NDVI difference and NDVI is likely responsible for the spatial patterns and temporal variations of global NDVI differences. The relationship is likely controlled by the spectral band adjustment factors in both the visible and near-infrared bands. Future work will focus on accurately determining these factors.

Acknowledgements

This study was financially supported in part by the State Key Program of National Natural Science Foundation of China under grant no. 41171272 and in part by the talent introduction project under grant no. NIGLAS2015QD08. We would like to thank Professor Tian Qingjiu with the International Institute for Earth System Sciences, Nanjing University, for his invaluable suggestions regarding this study. We also thank the anonymous reviewers and the editor for their constructive comments on an earlier version of this paper.

References

- Agapiou, A., Alexakis, D.D., Hadjimitsis, D.G., 2014. Spectral sensitivity of ALOS, ASTER, IKONOS, LANDSAT and SPOT satellite imagery intended for the detection of archaeological crop marks. *Int. J. Digit. Earth* 7 (5), 351–372.
- Brewin, R.J., Mélin, F., Sathyendranath, S., Steinmetz, F., Chuprin, A., Grant, M., 2014. On the temporal consistency of chlorophyll products derived from three ocean-colour sensors. *ISPRS J. Photogramm. Remote Sens.* 97, 171–184.
- Cao, C., Xiong, J., Blonski, S., Liu, Q., Upadhyay, S., Shao, X., Bai, Y., Weng, F., 2013. Suomi NPP VIIRS sensor data record verification, validation, and long-term performance monitoring. *J. Geophys. Res.: Atmos.* 118 (20), 11664–11678.
- Cavalli, R.M., Betti, M., Campanelli, A., Cicco, A.D., Guglietta, D., Penna, P., Piermattei, V., 2014. A methodology to assess the accuracy with which remote data characterize a specific surface, as a function of Full Width at Half Maximum (FWHM): application to three Italian coastal waters. *Sensors* 14 (1), 1155–1183.
- Clark, R.N., Swayze, G.A., Gallagher, A.J., King, T.V.V., Calvin, W.M., 1993. The U.S. Geological Survey, Digital Spectral Library: Version 1: 0.2 to 3.0 microns, U.S. Geological Survey Open File Report 93-592.
- Cracknell, A.P., 1997. *Advanced Very High Resolution Radiometer AVHRR*. CRC Press.
- Curier, R.L., Veefkind, J.P., Braak, R., Veihelmann, B., Torres, O., de Leeuw, G., 2008. Retrieval of aerosol optical properties from OMI radiances using a multiwavelength algorithm: application to western Europe. *J. Geophys. Res.* 13 (17S90).
- Curran, P.J., Williamson, H.D., 1986. Sample size for ground and remotely sensed data. *Remote Sens. Environ.* 20 (1), 31–41.
- Elvidge, C.D., 1990. Visible and infrared reflectance characteristics of dry plant materials. *Int. J. Remote Sens.* 11 (10), 1775–1795.
- Epiphanio, J.C.N., Huete, A.R., 1995. Dependence of NDVI and SAVI on sun/sensor geometry and its effect on FAPAR relationships in Alfalfa. *Remote Sens. Environ.* 51 (3), 351–360.
- Fan, X., Liu, Y., 2014. Quantifying the relationship between intersensor imagers in solar reflective bands: implications for intercalibration. *IEEE Trans. Geosci. Remote Sens.* 52 (12), 7727–7737.
- Fan, X., Liu, Y., Tao, J., Weng, Y., 2015. Soil salinity retrieval from advanced multispectral sensor with partial least square regression. *Remote Sens.* 7 (1), 488–511.
- Fan, X., Weng, Y., Tao, J., 2016. Towards decadal soil salinity mapping using Landsat time series data. *Int. J. Appl. Earth Obs. Geoinf.* 52, 32–41.
- Fan, Y., van den Dool, H., Mitchell, K., Lohmann, D., 2002. NWS-CPC's monitoring and prediction of US soil moisture and associated land surface variables: Land Data Renalysis. In: Proc. of the Climate Diagnostics Workshop, October 21–25.
- Friedl, M.A., McIver, D.K., Hodges, J.C.F., Zhang, X.Y., Muchoney, D., Strahler, A.H., Woodcock, C.E., Gopal, S., Schneider, A., Cooper, A., Baccini, A., Gao, F., Schaaf, C., 2002. Global land cover mapping from MODIS: algorithm and early results. *Remote Sens. Environ.* 83 (1), 287–302.
- Geiß, C., Pelizari, P.A., Marconcini, M., Sengara, W., Edwards, M., Lakes, T., Taubenböck, H., 2015. Estimation of seismic building structural types using multi-sensor remote sensing and machine learning techniques. *ISPRS J. Photogramm. Remote Sens.* 104, 175–188.
- Gonsamo, A., Chen, J.M., 2013. Spectral response function comparability among 21 satellite sensors for vegetation monitoring. *IEEE Trans. Geosci. Remote Sens.* 52 (3), 1319–1335.
- Gutman, G.G., 1991. Vegetation indices from AVHRR: an update and future prospects. *Remote Sens. Environ.* 35 (2), 121–136.
- Gutman, G., Ignatov, A., 1998. The derivation of the green vegetation fraction from NOAA/AVHRR data for use in numerical weather prediction models. *Int. J. Remote Sens.* 19 (8), 1533–1543.
- Holben, B.N., 1986. Characteristics of maximum-value composite images from temporal AVHRR data. *Int. J. Remote Sens.* 7 (11), 1417–1434.
- Hubanks, P., Platnick, S., King, M., Ridgway, B., 2015. MODIS atmospheric L3 gridded product algorithm theoretical basis document (ATBD) & users guide (Collection 006, Version 2.1 Beta, 6 May 2015).
- Ji, L., Zhang, L., Rover, J., Wylie, B.K., Chen, X., 2014. Geostatistical estimation of signal-to-noise ratios for spectral vegetation indices. *ISPRS J. Photogramm. Remote Sens.* 96, 20–27.
- Justice, C.O., Vermote, E., Townshend, J.R., Defries, R., Roy, D.P., Hall, D.K., Salomonson, V.V., Privette, J.L., Riggs, G., Strahler, A., Lucht, W., Myneni, R.B., Knyazikhin, Y., Running, S.W., Nemani, R.R., Wan, Z., Huete, A.R., van Leeuwen, W., Wolfe, R.E., Giglio, L., Muller, J.P., Lewis, P., Barnsley, M.J., 1998. The moderate resolution imaging spectroradiometer (MODIS): land remote sensing for global change research. *IEEE Trans. Geosci. Remote Sens.* 36 (4), 1228–1249.
- Kanamitsu, M., Ebisuzaki, W., Woollen, J., Yang, S.K., Hnilo, J.J., Fiorino, M., Potter, G.L., 2002. NCEP-DOE AMIP-II reanalysis (R-2). *Bull. Am. Meteorol. Soc.* 83 (11), 1631–1643.
- Huete, A., Didan, K., Miura, T., Rodriguez, E.P., Gao, X., Ferreira, L.G., 2002. Overview of the radiometric and biophysical performance of the MODIS vegetation indices. *Remote Sens.* 83 (1), 195–213.
- Kim, Y., Huete, A.R., Miura, T., Jiang, Z., 2010. Spectral compatibility of vegetation indices across sensors: band decomposition analysis with Hyperion data. *J. Appl. Remote Sens.* 4 (1), 043520.
- Levy, R.C., Remer, L.A., Kleidman, R.G., Mattoe, S., Ichoku, C., Kahn, R., Eck, T.F., 2010. Global evaluation of the Collection 5 MODIS dark-target aerosol products over land. *Atmos. Chem. Phys.* 10 (21), 10399–10420.
- Li, P., Jiang, L., Feng, Z., 2013. Cross-comparison of vegetation indices derived from Landsat-7 enhanced thematic mapper plus (ETM+) and Landsat-8 operational land imager (OLI) sensors. *Remote Sens.* 6 (1), 310–329.
- Liang, S., Fang, H., Chen, M., Shuey, C.J., Walhall, C., Daughtry, C., Morissette, J., Schaaf, C., Strahler, A., 2002. Validating MODIS land surface reflectance and albedo products: methods and preliminary results. *Remote Sens. Environ.* 83 (1), 149–162.
- Lunetta, R.S., Knight, J.F., Ediriwickrema, J., Lyon, J.G., Worthy, L.D., 2006. Land-cover change detection using multi-temporal MODIS NDVI data. *Remote Sens. Environ.* 105 (2), 142–154.

- Luo, Z., Kley, D., Johnson, R.H., Smit, H., 2008. Ten years of measurements of tropical upper-tropospheric water vapor by MOZAIC. Part II: assessing the ECMWF humidity analysis. *J. Clim.* 21 (7), 1449–1466.
- Maeda, E.E., Moura, Y.M., Wagner, F., Hilker, T., Lyapustin, A.I., Wang, Y., Chave, J., Möttus, M., Aragão, L.E.O.C., Shimabukuro, Y., 2016. Consistency of vegetation index seasonality across the Amazon rainforest. *Int. J. Appl. Earth Obs. Geoinf.* 52, 42–53.
- Martínez-Beltrán, C., Jochum, M.O., Calera, A., Melia, J., 2009. Multisensor comparison of NDVI for a semi-arid environment in Spain. *Int. J. Remote Sens.* 30 (5), 1355–1384.
- McPeters, R., Kroon, M., Labow, G., Brinksma, E., Balis, D., Petropavlovskikh, I., Veefkens, J.P., Bhartia, P.K., Levelt, P.F., 2008. Validation of the AURA Ozone Monitoring Instrument total column ozone product. *J. Geophys. Res.: Atmos.* 113 (D15).
- Moeller, C., Schwarting, T., McIntire, J., Oudrari, H., Moyer, D., 2011. NPP VIIRS Flight 1 Relative Spectral Response (RSR) Overview. University of Wisconsin.
- Michishita, R., Jin, Z., Chen, J., Xu, B., 2014. Empirical comparison of noise reduction techniques for NDVI time-series based on a new measure. *ISPRS J. Photogramm. Remote Sens.* 91, 17–28.
- Miura, T., Huete, A., Yoshioka, H., 2006. An empirical investigation of cross-sensor relationships of NDVI and red/near-infrared reflectance using EO-1 Hyperion data. *Remote Sens. Environ.* 100 (2), 223–236.
- Miura, T., Turner, J.P., Huete, A.R., 2013. Spectral compatibility of the NDVI across VIIRS, MODIS, and AVHRR: an analysis of atmospheric effects using EO-1 Hyperion. *IEEE Trans. Geosci. Remote Sens.* 51 (3), 1349–1359.
- Miura, T., Yoshioka, H., Fujiwara, K., Yamamoto, H., 2008. Inter-comparison of ASTER and MODIS surface reflectance and vegetation index products for synergistic applications to natural resource monitoring. *Sensors* 8 (4), 2480–2499.
- Nagol, J.R., Vermote, E.F., Prince, S.D., 2009. Effects of atmospheric variation on AVHRR NDVI data. *Remote Sens. Environ.* 113 (2), 392–397.
- Pinzon, J.E., Tucker, C.J., 2014. A non-stationary 1981–2012 AVHRR NDVI_{3g} time series. *Remote Sens.* 6 (8), 6929–6960.
- Pisek, J., Govind, A., Arndt, S.K., Hocking, D., Wardlaw, T.J., Fang, H., Matteucci, G., Longdoz, B., 2015. Intercomparison of clumping index estimates from POLDER, MODIS, and MISR satellite data over reference sites. *ISPRS J. Photogramm. Remote Sens.* 101, 47–56.
- Remer, L.A., Kaufman, Y.J., Tanré, D., Mattoe, S., Chu, D.A., Martins, J.V., Li, R.R., Ichoku, C., Levy, R.C., Kleidman, R.G., Eck, T.F., Vermote, E., Holben, B.N., 2005. The MODIS aerosol algorithm, products, and validation. *J. Atmos. Sci.* 62 (4), 947–973.
- Röder, A., Kuemmerle, T., Hill, J., 2005. Extension of retrospective datasets using multiple sensors. An approach to radiometric intercalibration of Landsat TM and MSS data. *Remote Sens. Environ.* 95 (2), 195–210.
- Roy, D.P., Lewis, P., Schaaf, C.B., Devadiga, S., Boschetti, L., 2006. The global impact of clouds on the production of MODIS bidirectional reflectance model-based composites for terrestrial monitoring. *IEEE Geosci. Remote Sens. Lett.* 3 (4), 452–456.
- Rahman, H., Dedieu, G., 1994. SMAC: a simplified method for the atmospheric correction of satellite measurements in the solar spectrum. *Int. J. Remote Sens.* 15 (1), 123–143.
- Ricotta, C., Avena, G., De Palma, A., 1999. Mapping and monitoring net primary productivity with AVHRR NDVI time-series: statistical equivalence of cumulative vegetation indices. *ISPRS J. Photogramm. Remote Sens.* 54 (5), 325–331.
- Rochdi, N., Fernandes, R., 2008. Intercalibration of Vegetation Indices from Landsat ETM+ and MODIS 500m Data for LAI mapping. Geomatics Canada, Chatham, ON, Canada, Technical Note, 3.
- Steven, M.D., Malthus, T.J., Baret, F., Xu, H., Chopping, M.J., 2003. Intercalibration of vegetation indices from different sensor systems. *Remote Sens. Environ.* 88 (4), 412–422.
- Tachiiri, K., 2005. Calculating NDVI for NOAA/AVHRR data after atmospheric correction for extensive images using 6S code: a case study in the Marsabit District, Kenya. *ISPRS J. Photogramm. Remote Sens.* 59 (3), 103–114.
- Teillet, P.M., Barker, J.L., Markham, B.L., Irish, R.R., Fedosejevs, G., Storey, J.C., 2001. Radiometric cross-calibration of the Landsat-7 ETM+ and Landsat-5 TM sensors based on tandem data sets. *Remote Sens. Environ.* 78 (1), 39–54.
- Teillet, P.M., Staenz, K., William, D.J., 1997. Effects of spectral, spatial, and radiometric characteristics on remote sensing vegetation indices of forested regions. *Remote Sens. Environ.* 61 (1), 139–149.
- Thenkabail, P.S., 2004. Inter-sensor relationships between IKONOS and Landsat-7 ETM+ NDVI data in three ecoregions of Africa. *Int. J. Remote Sens.* 25 (2), 389–408.
- Tian, F., Fensholt, R., Verbesselt, J., Grogan, K., Horion, S., Wang, Y., 2015. Evaluating temporal consistency of long-term global NDVI datasets for trend analysis. *Remote Sens. Environ.* 163, 326–340.
- Trishchenko, A.P., Cihlar, J., Li, Z.Q., 2002. Effects of spectral response function on surface reflectance and NDVI measured with moderate resolution satellite sensors. *Remote Sens. Environ.* 81 (1), 1–18.
- Trishchenko, A.P., 2009. Effects of spectral response function on surface reflectance and NDVI measured with moderate resolution satellite sensors: extension to AVHRR NOAA-17, 18 and METOP-A. *Remote Sens. Environ.* 113 (2), 335–341.
- Tucker, C.J., 1979. Red and photographic infrared linear combinations for monitoring vegetation. *Remote Sens. Environ.* 8 (2), 127–150.
- van Leeuwen, W.J., Orr, B.J., Marsh, S.E., Herrmann, S.M., 2006. Multi-sensor NDVI data continuity: uncertainties and implications for vegetation monitoring applications. *Remote Sens. Environ.* 100 (1), 67–81.
- Vermote, E.F., Tanre, D., Deuze, J.L., Herman, M., Morcette, J.J., 1997. Second simulation of the satellite signal in the solar spectrum, 6S: an overview. *IEEE Trans. Geosci. Remote Sens.* 35 (3), 675–686.
- Vermote, E.F., Vermeulen, A., 1999. Atmospheric correction algorithm: Spectral reflectances (MOD09). MODIS Algorithm Technical Background Document (version 4.0), NASA contract NAS5-96062.
- Volpi, M., Camps-Valls, G., Tuia, D., 2015. Spectral alignment of multi-temporal cross-sensor images with automated kernel canonical correlation analysis. *ISPRS J. Photogramm. Remote Sens.* (on line)
- Wu, G., Cui, L., Duan, H., Fei, T., Liu, Y., 2013. An approach for developing Landsat-5 TM-based retrieval models of suspended particulate matter concentration with the assistance of MODIS. *ISPRS J. Photogramm. Remote Sens.* 85, 84–92.
- Yang, F., Matsushita, B., Fukushima, T., Yang, W., 2012. Temporal mixture analysis for estimating impervious surface area from multi-temporal MODIS NDVI data in Japan. *ISPRS J. Photogramm. Remote Sens.* 72, 90–98.
- Yoshioka, H., Miura, T., Huete, A.R., 2003. An isoline-based translation technique of spectral vegetation index using EO-1 Hyperion data. *IEEE Trans. Geosci. Remote Sens.* 41 (6), 1363–1372.
- Zhang, G., Xiao, X., Dong, J., Kou, W., Jin, C., Qin, Y., Zhou, Y., Wang, J., Menarguez, M. A., Biradar, C., 2015. Mapping paddy rice planting areas through time series analysis of MODIS land surface temperature and vegetation index data. *ISPRS J. Photogramm. Remote Sens.* 106, 157–171.
- Zhu, Z., Bi, J., Pan, Y., Ganguly, S., Anav, A., Xu, L., Samanta, A., Piao, S., Nemani, R.R., Myneni, R.B., 2013. Global data sets of vegetation leaf area index (LAI) 3g and Fraction of Photosynthetically Active Radiation (FPAR)3g derived from Global Inventory Modeling and Mapping Studies (GIMMS) Normalized Difference Vegetation Index (NDVI3g) for the period 1981 to 2011. *Remote Sens.* 5 (2), 927–948.